Superstable lipid vacuoles endow cartilage with its shape and biomechanics

Raul Ramos [1 2], Kim T Pham [1 2], Richard C Prince [3 4], Leith B Leiser-Miller [5], Maneeshi S Prasad [6 7], Xiaojie Wang [1 2], Rachel C Nordberg [4], Benjamin J Bielajew [4], Jerry C Hu [4], Kosuke Yamaga [1 2], Ji Won Oh [1 2 8 9 10], Tao Peng [11 12], Rupsa Datta [4], Aksana Astrowskaja [13], Axel A Almet [11 14], John T Burns [1 2], Yuchen Liu [1 2], Christian Fernando Guerrero-Juarez [1 2 11 12], Bryant Q Tran [1 2], Yi-Lin Chu [1 2], Anh M Nguyen [1 2], Tsai-Ching Hsi [1 2], Norman T-L Lim [15], Sandra Schoeniger [16 17], Ruiqi Liu [1 2], Yun-Ling Pai [2 18], Chella K Vadivel [2 19], Sandy Ingleby [20], Andrew E McKechnie [21 22], Frank van Breukelen [23], Kyle L Hoehn [24], John J Rasweiler 4th [25], Michinori Kohara [26], William J Loughry [27], Scott H Weldy [28], Raymond Cosper [29], Chao-Chun Yang [30 31], Sung-Jan Lin [18], Kimberly L Cooper [32], Sharlene E Santana [5 33], Jeffrey E Bradley [33], Michael A Kiebish [34], Michelle Digman [12 35], David E James [36], Amy E Merrill [37], Qing Nie [11 12 14], Thomas F Schilling [1 12 14], Aliaksandr A Astrowski [38], Eric O Potma [3], Martín I García-Castro [6], Kyriacos A Athanasiou [4], Richard R Behringer [39], Maksim V Plikus [1 2 12 14]

[1] Department of Developmental and Cell Biology, University of California, Irvine, Irvine, CA, USA.

[2] Sue and Bill Gross Stem Cell Research Center, University of California, Irvine, Irvine, CA, USA.

[3] Department of Chemistry, University of California, Irvine, Irvine, CA, USA.

[4] Department of Biomedical Engineering, University of California, Irvine, Irvine, CA, USA.

[5] Department of Biology, University of Washington, Seattle, WA, USA.

[6] Division of Biomedical Sciences, School of Medicine, University of California, Riverside, Riverside, CA, USA.

[7] Department of Biochemistry, Jacobs School of Medicine and Biomedical Sciences, State University of New York at Buffalo, Buffalo, NY, USA.

[8] Department of Anatomy, College of Medicine, Yonsei University, Seoul, Republic of Korea.

[9] Department of Anatomy, School of Medicine, Kyungpook National University, Daegu, Republic of Korea.

[10] Biomedical Research Institute, Kyungpook National University Hospital, Daegu, Republic of Korea.

[11] Department of Mathematics, University of California, Irvine, Irvine, CA, USA.

[12] Center for Complex Biological Systems, University of California, Irvine, Irvine, CA, USA.

[13] Scientific Research Laboratory of Molecular Medicine, Grodna State Medical University, Grodna, Belarus.

[14] NSF-Simons Center for Multiscale Cell Fate Research, University of California, Irvine, Irvine, CA, USA.

[15] National Institute of Education, Singapore, Republic of Singapore.

[16] Institute of Veterinary Pathology, Leipzig University, Leipzig, Germany.

18 Discovery Life Sciences Biomarker Services GmbH, Kassel, Germany.

[18] Institute of Biomedical Engineering, College of Medicine and College of Engineering, National Taiwan University, Taipei, Taiwan.

[19] LEO Foundation Skin Immunology Research Center, Department of Immunology and Microbiology, University of Copenhagen, Copenhagen, Denmark.

[20] Australian Museum, Sydney, NSW, Australia.

[21] Mammal Research Institute, Department of Zoology and Entomology, University of Pretoria, Hatfield, South Africa.

[22] South African National Biodiversity Institute, Pretoria, South Africa.

[23] School of Life Sciences, University of Nevada, Las Vegas, Las Vegas, NV, USA.

[24] School of Biotechnology and Biomolecular Sciences, University of New South Wales, Sydney, NSW, Australia.

[25] Department of Obstetrics and Gynecology, SUNY Downstate Medical Center, New York, NY, USA.

[26] Department of Microbiology and Cell Biology, Tokyo Metropolitan Institute of Medical Science, Tokyo, Japan

[27] Valdosta State University, Valdosta, GA, USA.

[28] Serrano Animal and Bird Hospital, Lake Forest, CA, USA.

[29] Santa Ana Zoo, Santa Ana, CA, USA.

[30] Department of Dermatology, National Cheng Kung University Hospital, College of Medicine, National Cheng Kung University, Tainan, Taiwan.

[31] International Center for Wound Repair and Regeneration, National Cheng Kung University, Tainan, Taiwan.

[32] Department of Cell and Developmental Biology, University of California, San Diego, La Jolla, CA, USA.

[33] Department of Mammalogy, Burke Museum, University of Washington, Seattle, WA, USA.

[34] BPGbio, Inc., Framingham, MA, USA.

[35] Department of Chemical Engineering and Materials Science, University of California, Irvine, Irvine, CA, USA.

[36] Charles Perkins Centre, School of Life and Environmental Sciences and School of Medical Sciences, University of Sydney, Sydney, NSW, Australia.

[37] Center for Craniofacial Molecular Biology, Ostrow School of Dentistry, University of Southern California, Los Angeles, CA, USA.

[38] The Institute of Biochemistry of Biologically Active Compounds, Grodna, Belarus.

[39] Department of Genetics, The University of Texas MD Anderson Cancer Center, Houston, TX, USA.

Abstract

Conventionally, the size, shape, and biomechanics of cartilages are determined by their voluminous extracellular matrix. By contrast, we found that multiple murine cartilages consist of lipid-filled cells called lipochondrocytes. Despite resembling adipocytes, lipochondrocytes were molecularly distinct and produced lipids exclusively through de novo lipogenesis. Consequently, lipochondrocytes grew uniform lipid droplets that resisted systemic lipid surges and did not enlarge upon obesity. Lipochondrocytes also lacked lipid mobilization factors, which enabled exceptional vacuole stability and protected cartilage from shrinking upon starvation. Lipid droplets modulated lipocartilage biomechanics by decreasing the tissue's stiffness, strength, and resilience. Lipochondrocytes were found in multiple mammals, including humans, but not in nonmammalian tetrapods. Thus, analogous to bubble wrap, superstable lipid vacuoles confer skeletal tissue with cartilage-like properties without "packing foam-like" extracellular matrix.

Structured Abstract

INTRODUCTION:

Vertebrates have a complex endoskeleton that consists of cartilage and ossifying bones. The biomechanics of the collagen-rich extracellular matrix in cartilage underlie its physical integrity. Additionally, during embryonic development, vertebrates also form the notochord, an endoskeletal tissue that affords animal bodies with mechanical support through hydrostatics. The notochord maintains its shape and stiffness owing to its large cells, whose aqueous vacuoles resist compression. Remnants of the notochord in most vertebrates became the nucleus pulposus, a ball-like structure at the center of intervertebral disks.

RATIONALE

In this study, we noticed adipocyte-like cells featuring a giant lipid vacuole present throughout mouse ear cartilage. Yet, unlike adipocytes, these cells did not label with adipose-specific genetic markers. We chose to characterize this form of cartilage, called lipocartilage, which we found in vital anatomical structures of the nose, ear, larynx, and chest, and to establish whether its biomechanical properties depend on intracellular vacuoles.

RESULTS

We found that precursor cells for lipocartilage expressed transcriptional factors and extracellular matrix genes shared with the progenitors of “conventional” cartilage. During terminal differentiation, lipocartilage precursor cells activated lipid metabolism genes, including de novo lipogenesis enzymes that convert glucose to fatty acids. Lipocartilage formation depended on de novo lipogenesis to synthesize lipid vacuoles, and unlike adipocytes, its cells could not take up additional fatty acids from the circulation. Furthermore, compared with adipocytes, mature lipocartilage cells lacked enzymes needed to breakdown stored lipids, resulting in metabolically “locked” vacuoles. In fact, when adult mice were challenged with either caloric restriction or a high-fat diet, their external ears and the lipid vacuoles contained within them did not change in size. This was in contrast to adipose tissues, which readily emptied or filled their lipid vacuoles, respectively. Beyond rodents, we identified lipocartilage in phylogenetically diverse mammals, including in the ears of echolocating bats, where it becomes particularly intricate. Abundant lipid droplets also form in human cartilage cells grown in vitro from embryonic stem cells.

CONCLUSION

We postulate that lipocartilage is a distinct type of vacuolated skeletal tissue that has evolved in mammals and is similar in form and function to vacuolated notochord. Lipocartilage attains and maintains its size and shape by adapting a distinct lipid metabolism program that enables the formation of superstable lipid vacuoles. Skeletal elements made of lipocartilage commonly acquire complex, micropatterned shapes, such as in elaborately shaped bat ears. Our lipid washout assays further suggest that vacuoles are critically required for lipocartilage biomechanics, calling for in-depth studies on the structure-function relationship between intracellular vacuoles versus extracellular matrix in skeletal tissues. Regenerative medicine strategies for embryonic stem cell–derived human cartilage can use lipid vacuoles as a natural biomarker that distinguishes differentiated cells from pluripotent progenitors.

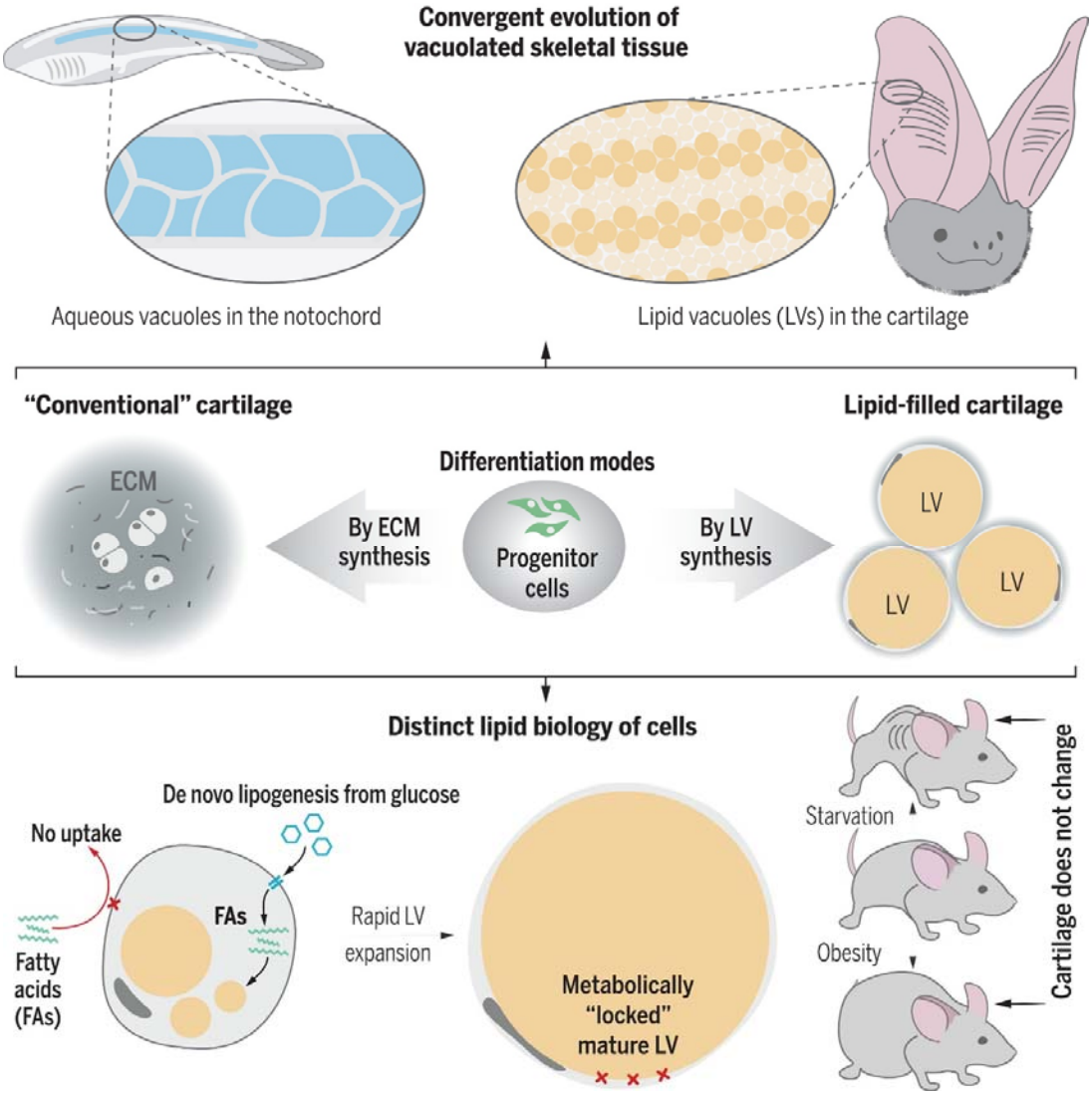

Lipid-filled cartilage of mammals.

Unlike in conventional cartilage, the form and function of lipid-filled cartilage derives from giant lipid vacuoles (center). Vacuolated cartilage in mammals represents convergent evolution with the notochord, which has cells containing giant aqueous vacuoles. Developing cartilage grows vacuoles by a tightly controlled biochemical pathway (bottom). Mature lipocartilage maintains stable vacuoles by turning off lipid mobilization. This unusual molecular biology safeguards the vacuoles from unintended size fluctuations upon systemic metabolic disturbances. ECM, extracellular matrix.

Cartilage forms an essential component of the vertebrate skeletal system, playing critical mechanical and morphogenetic roles (*1*). Connective tissues similar to cartilage also exist in multiple invertebrate groups, including annelids, cephalopods, and horseshoe crabs (*2*, *3*). Conventionally, differentiated cells called chondrocytes secrete large quantities of extracellular matrix (ECM), which endows cartilage with its biomechanical properties. During embryogenesis, cartilage arises from both mesodermal and neural crest sources (*4*, *5*), and, in some cranial cartilage, cells from these two embryonic origins can join together (*6*, *7*).

During our studies on mouse ear skin (*8*), we noticed prominent "lipid ghost" artifacts in ear cartilage after histological processing. Lipid ghosts are characteristic histological artifacts in adipose tissue but are uncommon in other healthy tissue types, where cells lack large lipid vacuoles. Intrigued by this finding, we found that mice have multiple sites of lipid-laden cartilage (referred to hereafter as lipocartilage) consisting of vacuolated, adipocyte-like cells called lipochondrocytes (LCs). First observed by Franz von Leydig in the 1850s (fig. S1, A and B) (*9*), LCs were again described in a handful of histological studies more than 100 years later (*10*–*13*). However, along with Leydig's original discovery, these studies remain obscure, and virtually nothing is known about LCs' cellular lineage, biochemistry, biomechanics, gene regulatory program, or function, despite their prevalence in many vital skeletal structures.

Lipocartilage is lipid-filled, long-lived tissue

We comprehensively profiled mouse cartilage for the presence of LCs (Fig. 1A and fig. S1, C to G). In the head and neck, many cartilage structures arise from the neural crest cells (*7*) that express *Wnt1* and label with *Wnt1-Cre2* genetic construct (*14*). In *Wnt1-Cre2;mT/mG* mice, in which *Wnt1*-expressing cells and their progenies become stably green fluorescent protein (GFP) reporter positive, the nasal cartilage expressed GFP (*n* = 5 mice) (Fig. 1B) and consisted of vacuolated cells that stained with neutral lipid dye OilRedO (*n* = 3) (Fig. 1, C and D). The larynx, a complex organ in the neck, was made up of neural crest–derived epiglottic, non–neural crest–derived cricoid and arytenoid, and composite thyroid cartilages (*n* = 5) (Fig. 1, E and F) (*15*). With exception of the non–neural crest portion of the thyroid cartilage, we found lipid-laden cells in all laryngeal cartilage elements analyzed (*n* = 3) (Fig. 1, G and H, and fig. S1E). Lipid-filled cells also constituted the xiphoid cartilage of the sternum (*n* = 5) (fig. S1, F and G). Ear cartilage stained strongly with OilRedO (*n* = 8) (Fig. 1, I to K) and the fluorescent neutral lipid dye BODIPY (*n* = 3) (Fig. 1L). Its lipid-filled cells were highly uniform in size (fig. S2, A and B) and organized into a thin plate, two to three cell diameters across (movie S1). In many places, the ear cartilage plate had fenestrae (Fig. 1, I to K), commonly traversed by small blood vessels (fig. S3A) and occupied by clusters of large lipid-filled cells (Fig. 1K and fig. S2). In *Wnt1-Cre2;R26R* mice (*n* = 4) (fig. S2C) and cartilage-specific *Col2a1-CreER^{T2};R26R* mice (*n* = 3) (fig. S2D), in which Cre-expressing cells stably activate β-galactosidase and label with X-gal dye, only lipid-laden cells in the plate—but not those in fenestrae—were lacZ positive. Conversely, in adipocyte-specific *Retn-lacZ* (*n* = 4) (fig. S2E) and *Adipoq-Cre;R26R* mice (*n* = 6) (fig. S2F), only lipid-filled cells of fenestrae expressed lacZ. Thus, LCs are prevalent across numerous cartilages and have an embryonic origin that is distinct from that of similar-looking bona fide adipocytes.

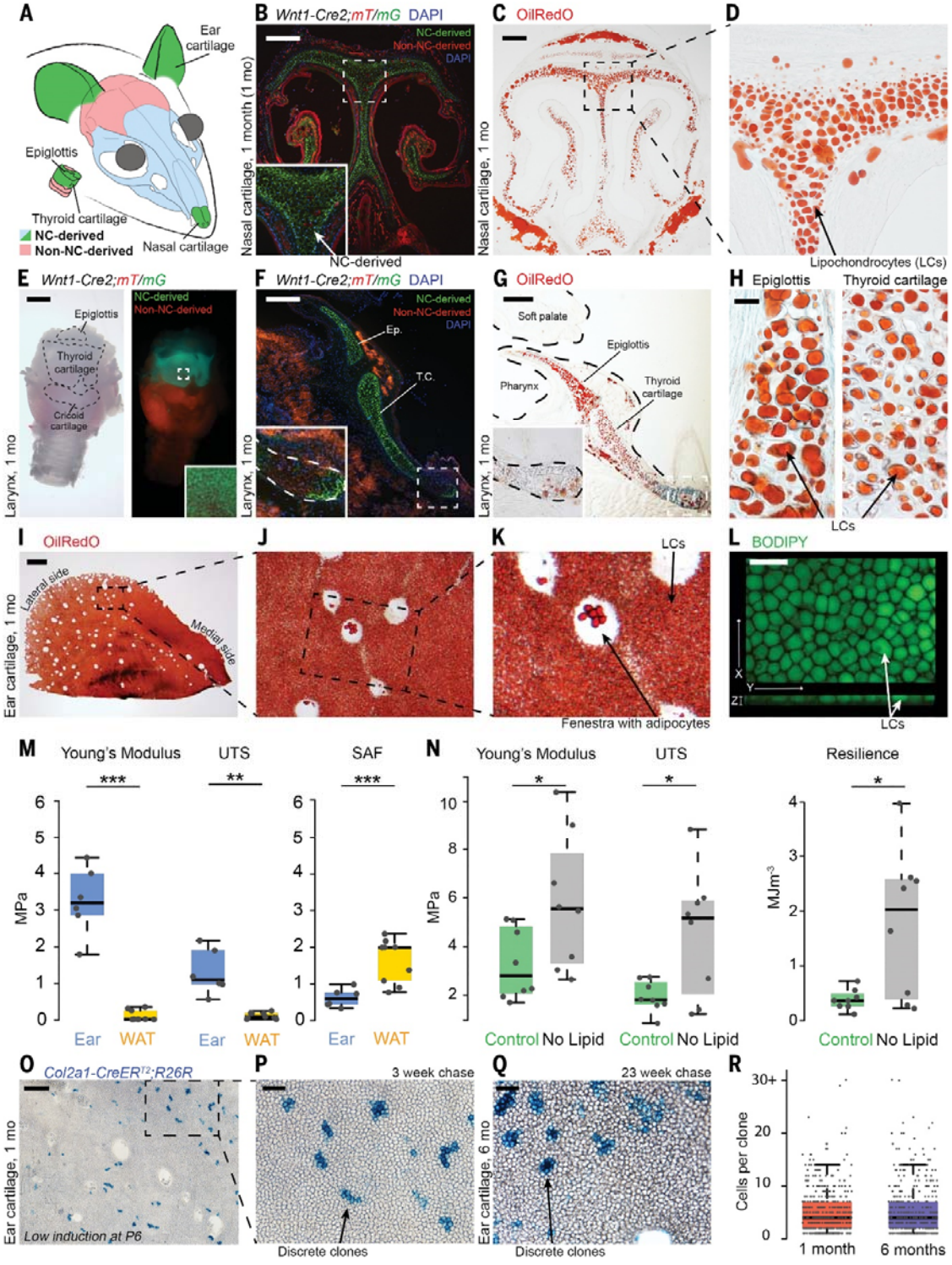

Fig. 1. LCs are present in multiple cartilages and impart biomechanical properties.

(**A**) Schematic drawing of mouse cartilages, color-coded by embryonic origin. LC-containing neural crest (NC)–derived lipocartilage is shown in green. (**B** to **H**) OilRedO staining and lineage tracing in *Wnt1-Cre2;mT/mG* mice show lipid-laden LCs in NC-derived nasal [(B) to (D)] and epiglottic and thyroid cartilage [(E) to (H)], except for the posterior end [insets in (F) and (G)]. See fig. S2. (**I** to **L**) Ear lipocartilage consists of OilRedO^{+} and BODIPY^{+} LCs and contains fenestrae occupied by adipocytes. (**M**)

Biomechanical analyses of mouse ear lipocartilage (ear) compared with WAT. Despite morphological similarities, lipocartilage displays significantly higher stiffness (Young's modulus) (left; 3.25 ± 0.38 MPa; Welch's *t* test, ***P = 0.0004) and UTS (center; 1.30 ± 0.24 MPa; Welch's *t* test, **P = 0.005) compared with WAT but lower strain at failure (SAF) (right; 0.60 ± 0.10; ***P = 0.0273). (**N**) Biomechanical analyses of native rat ear lipocartilage (control) and delipified tissue. Compared with control (green), stiffness (left; 3.27 ± 0.52 versus 5.79 ± 0.99 MPa; Welch's *t* test, *P = 0.0004), UTS (center; 1.91 ± 0.22 versus 4.53 ± 0.92 MPa; Welch's *t* test, *P = 0.0259), and resilience (right; 0.38 ± 0.06 versus 1.77 ± 0.48 MJm^{-3}; Welch's *t* test, *P = 0.0228) increase significantly after delipification (gray). (**O** to **R**) Clonogenic analysis in *Col2a1-CreER^{T2};R26R* mice shows that lacZ-labeled LCs form discrete clones that are stable in size for 6 months (Kolmogorov-Smirnov test, P = 0.506). Scale bars: 25 μm (H); 100 μm [(L), (P), and (Q)]; 200 μm [(B), (C), and (F)]; 250 μm (G); 500 μm (O); 1 mm [(E) and (I)].

We next examined LCs' longevity. Low-dose tamoxifen treatment of *Col2a1-CreER^{T2};R26R* mice at postnatal day P6 recombined individual lipocartilage progenitors, leading to discretely labeled LC clones in adult ears (Fig. 1O). LC clone sizes 3 weeks (n = 449 clones) (Fig. 1P) and 23 weeks after labeling (n = 384 clones) (Fig. 1Q) were not significantly different (P = 0.506) (Fig. 1R). Furthermore, large BODIPY$^+$ LCs persisted in the noses of aged mice (n = 4) and the ears of aged rats (n = 6) (fig. S4), which supports the notion that LCs are long-lived cells with a limited turnover rate.

Lipid droplets modulate tissue biomechanics

Next, we performed a series of uniaxial tensile tests to compare biomechanical properties of 1-month-old ear lipocartilage (n = 6), inguinal white adipose tissue (WAT) (n = 9), knee meniscus (n = 7), and rib cartilage (n = 8) (*16*). Young's modulus and ultimate tensile strength (UTS) values of lipocartilage (3.25 ± 0.38 and 1.30 ± 0.24 MPa, respectively) were significantly higher than those of WAT [0.11 ± 0.04 MPa (P = 0.0004) and 0.11 ± 0.02 MPa (P = 0.005), respectively] (Fig. 1M), which indicates a greater ability of lipocartilage to resist deformation and tear. Lipocartilage also showed significantly lower strain at failure values (0.60 ± 0.1) compared with adipose (1.61 ± 0.19; P = 0.0008) (Fig. 1M). By contrast, ECM-rich and lipid-devoid cartilage from the knee meniscus and rib showed significantly higher Young's modulus (23.94 ± 5.14 and 23.86 ± 4.32 MPa, respectively) and UTS values (9.86 ± 2.61 and 11.01 ± 1.91 MPa, respectively) that fell within previously reported values for fibrous and hyaline cartilages (fig. S5) (*17*, *18*). We then investigated whether the removal of lipid vacuoles would significantly alter lipocartilage biomechanics. Chloroform and methanol treatment efficiently emptied lipid droplets from LCs and delipified microdissected rat ear lipocartilages (fig. S6). Delipified lipocartilages (n = 8) showed altered biomechanical parameters compared with their native state (n = 8)—Young's modulus, UTS, and resilience values significantly increased [3.27 ± 0.52 versus 5.79 ± 0.99 MPa (P = 0.0004), 1.91 ± 0.22 versus 4.53 ± 0.92 MPa (P = 0.0259), and 0.38 ± 0.06 versus 1.77 ± 0.48 MJm^{-3} (P = 0.0228), respectively] (Fig. 1N), which suggests that lipid vacuoles conferred compliance to cartilage. Notably, in their delipified state, lipocartilage properties shifted toward values displayed by naturally lipid-devoid and ECM-rich murine meniscus and rib cartilages (fig. S5). Thus, lipid vacuoles impart distinct biomechanical properties to lipocartilages.

Lipocartilage has distinctive molecular properties

Next, we examined what molecular features characterize lipocartilage and how they may differ from those in WAT. We started by comparing whole-tissue lipidomic profiles of 1-month-old ear lipocartilage (*n* = 5) and inguinal WAT (*n* = 5) (Fig. 2A and fig. S7, A to E). On analysis, neutral lipids appeared as the dominant molecular species of both tissues owing to the large size and abundance of their lipid vacoles (Fig. 2B). With this in mind, we found that the composition of lipocartilage vacuoles differs from that of WAT. In WAT, 86.5% of neutral lipids were triglycerides. However, in lipocartilage, triglycerides constituted only 43.3% of neutral lipids and 31.1% (three times as high as in WAT) were fatty acid esters of hydroxy fatty acids (FAHFAs)—a class of neutral lipids with anti-inflammatory properties (*19*). Compositional lipidome differences between lipocartilage and WAT extended across all classes of lipids beyond triglycerides and FAHFAs (fig. S7F). Furthermore, compared with WAT (3.8%), lipocartilage lipids also contained significantly more saturated fatty acid chains (19.7%), the main product of de novo lipogenesis (Fig. 2C, fig. S7, and table S1). Thus, lipid vacuoles in lipocartilage are produced using metabolic pathways distinct from those in WAT.

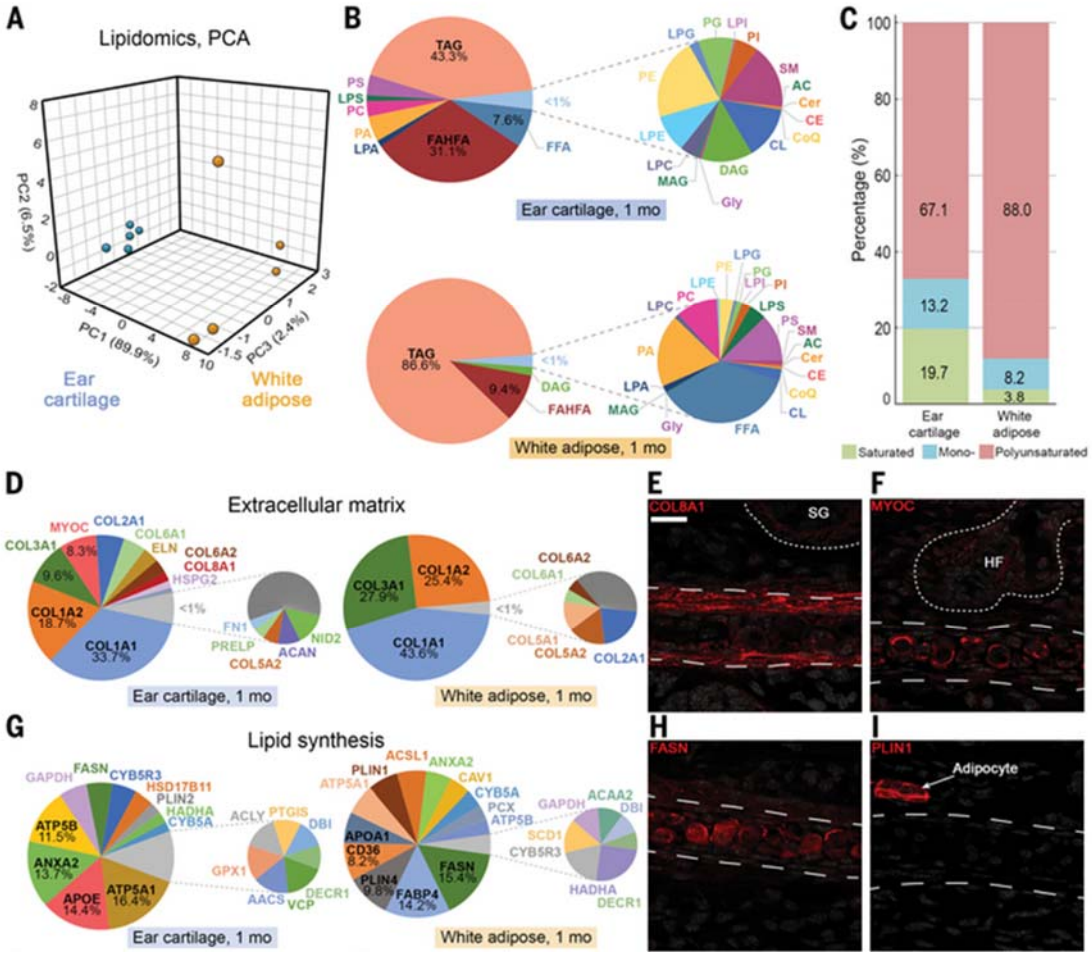

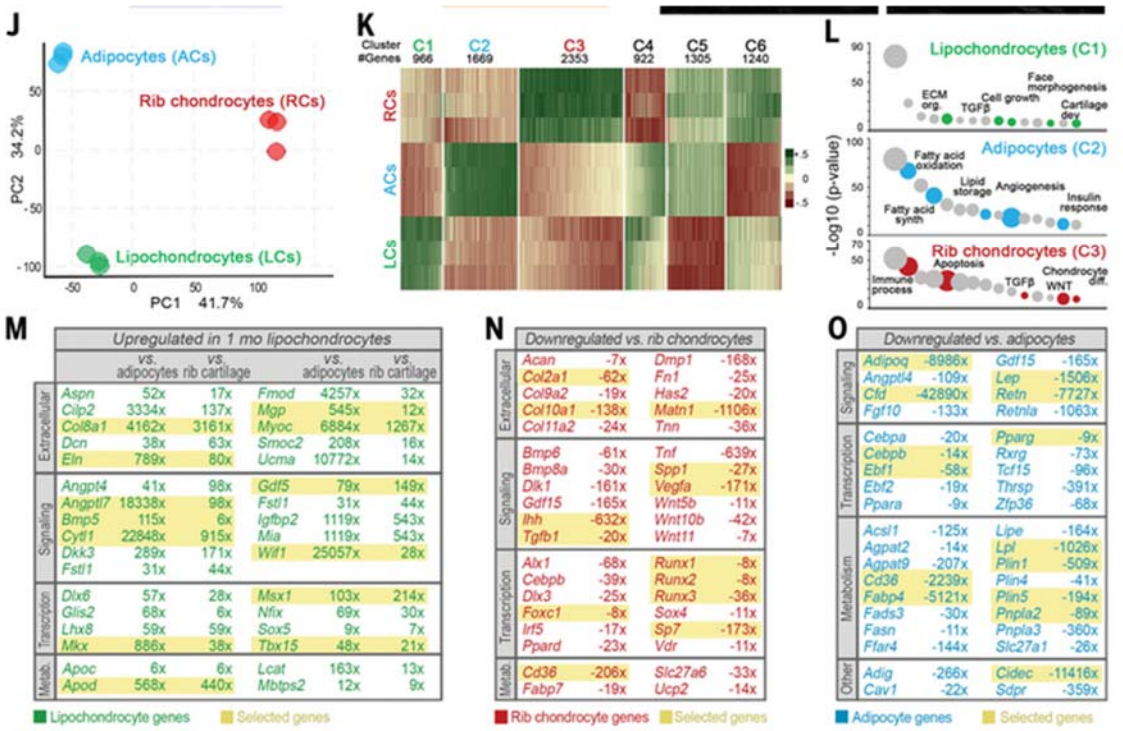

Fig. 2. LCs have a distinctive multiomic profile.

(**A**) Lipidomic profile of ear lipocartilage (blue) is distinct from that of inguinal WAT (yellow) on principal components analysis (PCA). (**B**) Lipocartilage and WAT are differentially enriched for distinct lipid classes. See table S1 for the definition of lipid classes. Prominently, lipocartilage is enriched for free fatty acids (FFAs) and FAHFAs, whereas WAT is enriched for triacylglycerols (TAGs) and diacylglycerols (DAGs). (**C**) Compared with WAT, lipocartilage contains substantially more lipids with saturated FFA tails (green). (**D** to **I**) Proteomic [(D) and (G)] and immunostaining analyses [(E), (F), (H), and (I)] show marked differences in structural and lipogenesis protein content between ear lipocartilage and WAT. Prominently, lipocartilage is enriched for COL8A1 and MYOC (D), which have distinct localization patterns [(E) and (F)]. SG, sebaceous gland; HF, hair follicle. (**J** and **K**) PCA and heatmap analyses show that transcriptional signature of ear LCs (green) is distinct from that in adipocytes (blue) and rib hyaline chondrocytes (red). See table S3. (**L**) All three cell types show distinct enrichments for gene ontology terms. See table S4. (**M** to **O**) List of selected genes differentially up-regulated in LCs (M), rib chondrocytes (N), or adipocytes (O) are shown. See table S3. Scale bars: 20 μm [(E), (F), (H), and (I)].

We then compared ear lipocartilage (n = 3) and WAT (n = 3) using whole-tissue mass spectrometry (table S2). In both tissues, we separately studied ECM proteins, which dominate upon analysis, as well as those involved in lipid metabolism. Lipocartilage and WAT displayed significant compositional differences in both protein categories. WAT ECM was dominated by collagen I and III subunits (COL1A1, 1A2, and 3A1), which collectively accounted for 97% of all detected ECM proteins (Fig. 2D). By contrast, these three collagens constituted only 62.2% of ECM proteins in lipocartilage, which also featured signature cartilage proteins COL2A1, 6A1, 6A2, and elastin as well as ECM proteins normally not associated with cartilage, myocilin (8.4%) and collagen COL8A1 (2%). On immunostaining, COL8A1 dominantly localized to the lipocartilage plate periphery, whereas myocilin surrounded individual mature LCs (Fig. 2, E

and F, and fig. S3B). In the lipid metabolism category, the topmost abundant factors in WAT were de novo lipogenesis enzyme fatty acid synthase (FASN) (15.5%), fatty acid binding protein FABP4 (14.3%), lipid mobilization proteins PLIN4 (9.8%) and PLIN1 (6.6%), and fatty acid transporter CD36 (8.2%) (Fig. 2G). Of these, only FASN (5.4%) was significantly detectable in lipocartilage by immunostaining (Fig. 2, H and I). Other topmost lipid metabolism factors in lipocartilage were apolipoprotein E (APOE) (14.5%) and PLIN2 (2.4%). Notably, the third-most-abundant protein in lipocartilage was vimentin, known for forming intermediate filament cages around early lipid vacuoles (*20*). Vimentin was 15 times as abundant in lipocartilage compared with WAT. Thus, despite sharing a similar morphology, both tissues have distinct ECM composition and substantial differences in lipid biogenesis machinery.

Next, we compared adult isolated ear LCs (n = 3), WAT adipocytes (n = 3), and rib hyaline cartilage chondrocytes (n = 3) (*21*) using RNA sequencing (RNA-seq). The LC transcriptome was distinct from those of adipocytes and hyaline chondrocytes (Fig. 2J), with 8455 differentially expressed genes (Fig. 2K and table S3). Each cell type was enriched for specific gene ontology terms (table S4), with LCs simultaneously enriched for cartilage and metabolic terms (Fig. 2L). Both LCs and hyaline chondrocytes expressed many of the same ECM genes that were otherwise minimally present in adipocytes (table S3) yet also showed significant cartilage type–specific enrichment patterns (Fig. 2, M and N). Matching our proteomic data, LCs expressed particularly high levels of *myocilin* and *Col8a1*. Significant expression differences between LCs and hyaline chondrocytes extended across signaling molecules and transcriptional regulators (Fig. 2, M and N; see also Materials and methods, Gene expression analysis section). Matching and expanding on our proteomic results, LC and adipocyte transcriptomes prominently diverged within the metabolic category. Unlike adipocytes, LCs did not express adipokines *Adipoq*, *Cfd* (*adipsin*), *Lep*, *Retn*, and *Retnla* and proadipogenic transcriptional regulators *Ebf1*, *Ebf2*, *Cebpb*, *Ppara*, *Rxrg*, and *Thrsp* (Fig. 2O and table S3). Differences extended to multiple key genes involved in lipid biosynthesis and catabolism as well as lipid vacuole formation and maintenance. LCs did not express *Cd36* and expressed low levels of *Slc27a1*, two major fatty acid transporters in adipocytes. However, glucose transporters, including *Slc2a1* and *Slc2a4*, and key de novo lipogenesis enzymes *Acly*, *Acaca*, *Fasn*, and *Scd1* were expressed. LCs also expressed many key enzymes required at all steps of triglyceride synthesis (table S3). Notably, *Pnpla2*, *Lipe*, and *Mgll*, key enzymes required for triglyceride mobilization and breakdown, were expressed at very low levels in LCs. Also, not expressed and down-regulated, respectively, were *Plin1* and *Abhd5*, both of which are critical for hormone-stimulated lipolysis in adipocytes (table S3). Finally, LCs expressed several key proteins implicated in lipid vacuole assembly, fusion, and stability, albeit many of them at reduced levels as compared with adipocytes (table S3). We validated selected differentially expressed metabolic genes by quantitative real-time polymerase chain reaction (qRT-PCR) and by in situ RNA staining (fig. S8). Thus, our combined multiomic profiling reveals that lipocartilage is a distinct skeletal tissue type whose ECM only partially resembles conventional cartilage ECM and whose lipid-filled cells lack many essential fat biogenesis genes otherwise expressed by metabolically active adipocytes.

Lipocartilage differentiates through lipogenesis

We next investigated when during their development that lipocartilage activates the lipogenesis program. Distinct forms of lipocartilage in mice develop asynchronously—for example, although nasal LC formed lipid droplets during embryonic development, starting from embryonic day E13.5 (fig. S9), ear LC did so with a substantial delay, starting around postnatal day P10 (fig. S10, I to M). Given its accessibility and ease of microdissection, we profiled ear lipocartilage development in-depth. By examining morphological changes (fig. S10, A and B), coexpression patterns of chondrogenic marker SOX9 and proliferation marker proliferating cell nuclear antigen (PCNA) (fig. S10, C to H) as well as SOX9 and EdU incorporation (fig. S11), and lipid vacuole marker OilRedO (fig. S10, I to M), we established the following key morphogenetic events: P4 as the onset of chondrogenic commitment by ear pinna mesenchyme; P8 and P10 as the early and late proliferative phases, respectively; P13 as the transition phase; and P21 and 1 month as the early and late differentiation phases, respectively (Fig. 3A). We then studied LCs and their progenitors at five time points using RNA-seq. Between P8 and P13, we sorted LC progenitors as tdTomato^{hi} cells from microdissected *Wnt1-Cre2;tdTomato* cartilage primordia (fig. S12, A and B). At P21 and 1 month, lipid-containing LCs were isolated by buoyancy. The LC transcriptome prominently changed with time (n = 3 per time point; Fig. 3B), and 2397 differentially expressed genes organized into four time-dependent clusters (Fig. 3C and table S5). Cluster T1 genes up-regulated during the proliferative phase; T2 genes during the transition phase; and T3 and T4 genes during the early and late differentiation phases, respectively. Gene category (table S6) and gene ontology enrichment analyses (table S7) showed that cell cycle activators and promitotic factors were abundant in LC progenitors and then largely shut down upon differentiation (Fig. 3D, teal). By contrast, cell cycle inhibitors were enriched in late differentiated LCs. Lipogenesis genes, including *Dgat2*, *Fasn*, *Lpin1*, and *Mogat1*, prominently increased at the onset of LC differentiation (Fig. 3D, orange), whereas other critical lipogenesis factors, including *Agpat2*, *Agpat3*, *Bscl2*, *Cidea*, *Dgat1*, *Fabp5*, *Mogat2*, and *Plin2*, were enriched in late differentiated LCs (table S6). Transcription factors (Fig. 3D, jade) and ECM genes (Fig. 3D, purple) showed early and late enrichment peaks. Early transcription factors included neural crest–derived mesenchyme regulator *Hes1* and chondrogenesis regulators *Sox6* and *Sox8*. Late transcription factors included known lipogenesis activators *Klf15*, *Srebf1*, *Stat5a*, and *Stat5b* (table S6). Early ECM genes included established cartilage-specific collagens *Col2a1*, *9a1*, *9a2*, and *11a2* as well as *elastin*, *fibulin 5*, *fibrilin 2*, and *periostin*, whereas late ECM genes included collagens *Col8a1* and *Col10a1* as well as *chondroadherin*, *fibrilin 1*, and *myocilin* (fig. S12, C and D, and table S6). Signaling factors showed complex temporal patterns across several major pathways, including bone morphogenetic protein (BMP), insulin-like growth factor (IGF), transforming growth factor–β (TGFβ), and WNT (table S6). Thus, the lipocartilage developmental program is dominated by cell cycle genes, prochondrogenic transcription, and ECM factors during its early phase and by lipogenesis machinery and specialized ECM proteins in the late phase.

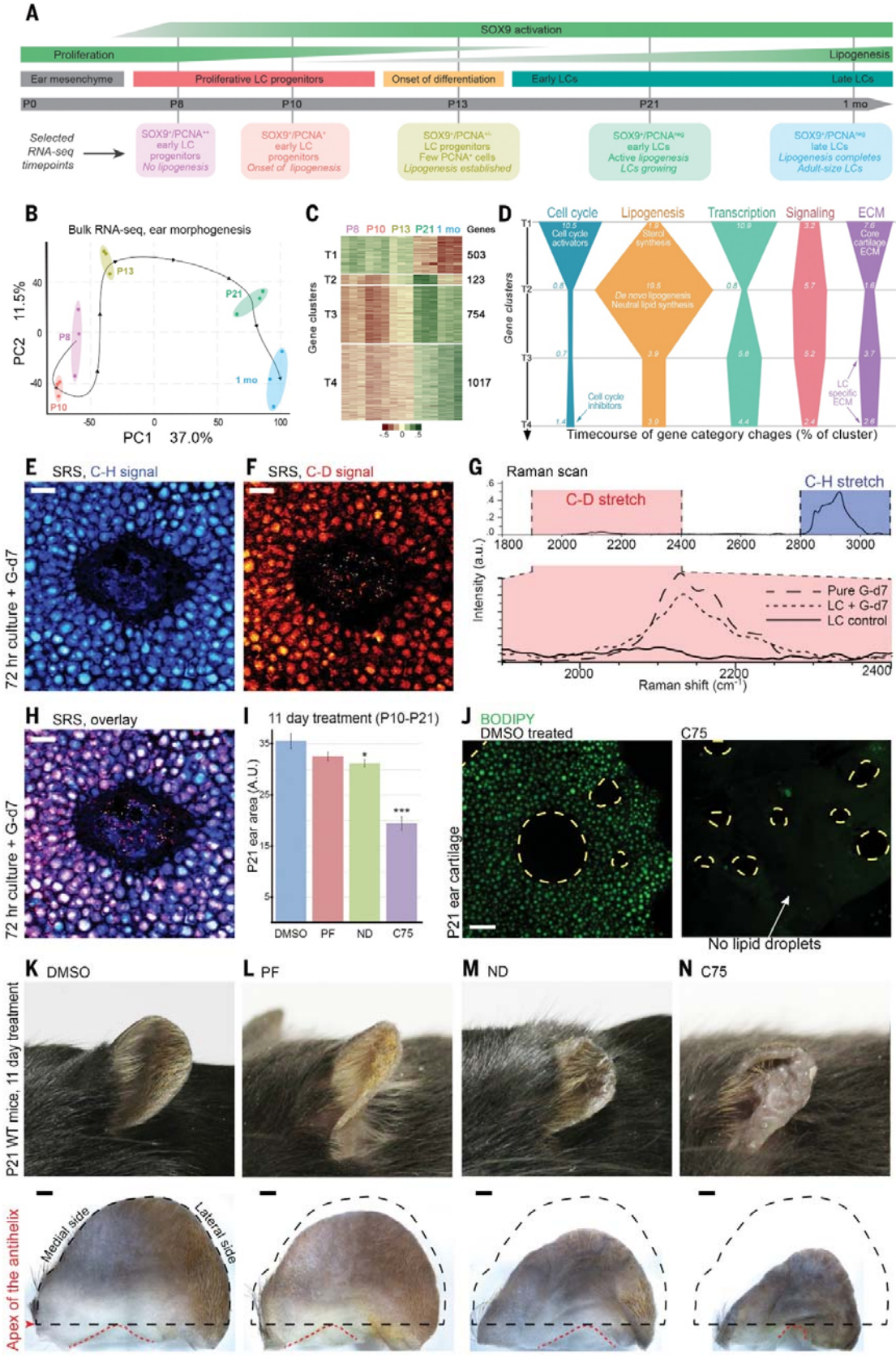

Fig. 3. Lipocartilage activates and depends on de novo lipogenesis.

(**A**) Schematic summary of the key stages and cellular events in ear lipocartilage development. RNA-seq time points are defined and annotated. (**B** and **C**) PCA and heatmap analyses show transcriptional changes in developing ear LCs at selected postnatal time points. See table S5. (**D**) Relative abundance of genes across clusters T1 to T4 from (C) within selected gene categories. (**E** to **H**) SRS analysis reveals that glucose-derived deuterium (also known as heavy hydrogen atom) incorporates into lipid vacuoles of developing ear LCs. Color-coded images of ear cartilage reveal total lipid within carbon-hydrogen bond (C-H) vibration range (E) and de novo lipogenesis-derived lipid within carbon-deuterium bond (C-D) vibration range (F). Raman scan on LC lipid vacuoles cultured in the presence of deuterated glucose (G-d7) shows C-H stretch peak, common to lipids, as well as a C-D stretch peak that overlaps with the C-D peak of pure G-d7 [(G), red region]. An overlay of (E) and (F) is shown in (H). (**I** to **N**) Ears become smaller in mice topically treated with de novo lipogenesis inhibitors PF-05175157 (PF), ND-646 (ND), and C75 as compared with DMSO control (I). C75-treated ears show prominent decrease in $BODIPY^+$ lipid vacuoles (J). Representative mice and dissected 1-month-old ears are shown in (K) to (N). WT, wild-type; A.U., arbitrary units. $*P < 0.0042$; $***P < 0.0001$. Scale bars: 25 μm [(E), (F), and (H)]; 50 μm (J); 2 mm [(K) to (N)].

Because the growth of lipid vacuoles in LCs resulted in a form of cellular hypertrophy, we asked whether lipocartilage activates canonical cartilage hypertrophy genes and forms templates for mineralizing bones. Unlike rib chondrocytes, LCs did not express cartilage hypertrophy markers *Alpl*, *Ihh*, and *Runx2* on RNA-seq (fig. S13). Staining of the embryonic nasal capsule for BODIPY and ossification marker collagen COLX in E13.5 to E15.5 mice (fig. S9) and spatial sequencing analysis in E16.5 mice (fig. S14) showed that differentiating nasal lipocartilage was sharply demarcated from nasal septum bone and did not activate the ossification gene program. Thus, lipocartilage does not ossify, and LC differentiation is distinct from canonical chondrocyte hypertrophy through cytoplasmic swelling.

LCs are metabolically refractory

LCs did not express *Cd36* and prominently down-regulated *Slc27a1*, both of which are necessary for dietary fatty acid uptake in adipocytes (Fig. 2O, figs. S10B and S15, and table S3). Furthermore, genes necessary for fatty acid mobilization from lipid stores were either not expressed—*Plin1*—or strongly down-regulated—*Abhd5*, *Lipe*, *Mgll*, and *Pnpla2* (fig. S15 and table S3). This prompted us to test how LCs respond to fluctations in dietary lipid availability. We studied ear morphology and LC size in mice after 12 weeks of high-fat diet or 72 hours of restricted caloric intake. Compared with mice fed regular chow ($n = 6$), ear size (Fig. 4A, top, versus Fig. 4, B and D, top) and lipid droplet size (Fig. 4A, bottom, versus Fig. 4, B and C, bottom) did not change significantly in mice fed a high-fat diet ($n = 6$; $P > 0.9999$ and $P > 0.1966$, respectively) (Fig. 4, E and F). This was despite significant increases in body weight ($P = 0.0008$) (Fig. 4G) and dermal and perigonadal WAT adiposity (fig. S16, A and B). Similarly, obese leptin receptor–null mice (*db/db*; $n = 6$) showed a significant increase in body weight ($P > 0.0005$) and WAT adiposity (fig. S16D) but no significant changes in ear size ($P = 0.1733$) (Fig. 4E) or LC size ($P = 0.9261$) (Fig. 4F). Mice on restricted caloric intake ($n = 3$) also did not show significant ear or LC size changes ($P > 0.9999$ and $P > 0.6033$, respectively) (Fig. 4, C, E, and F), even though their body weight ($P = 0.0277$) (Fig. 4G) and WAT adiposity reduced significantly (fig. S16C). Thus, unlike WAT, lipocartilage is protected from systemic fluctuations in dietary lipid availability.

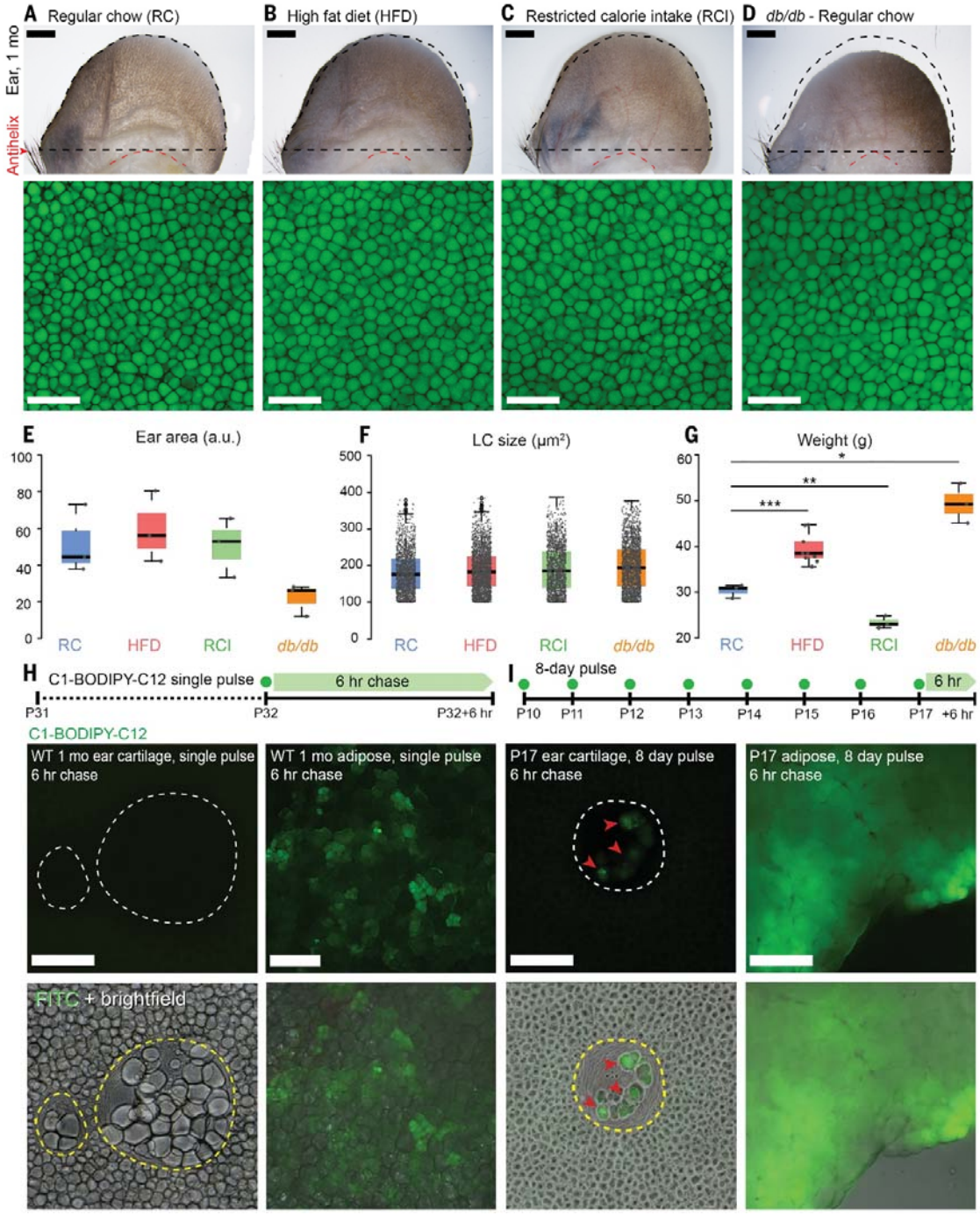

Fig. 4. Lipocartilage maintains superstable lipid vacuoles.

(**A** to **D**) Ears (top) and individual LCs (bottom) do not significantly change in size in mice on a high-fat diet (HFD), obese *db/db* mice, or mice on restricted calorie intake (RCI) as compared with mice fed regular chow (RC). Representative images are shown. (**E** to **G**) In contrast to ear size [Welch's analysis of variance (ANOVA), $P = 0.0966$] (E) and LC size (one-way ANOVA, $P = 0.2419$) (F), body weight (Welch's ANOVA, $P = 0.0002$) (G) as well tissue adiposity (see fig. S16) significantly increase in HFD (39.43 ± 1.10 g; Dunnett's T3, $P = 0.0005$) and *db/db* animals (49.36 ± 2.51 g; Dunnett's T3, $P = 0.0396$) and decrease in RCI conditions (23.38 ± 0.79 g; Dunnett's T3, $P = 0.0100$) relative to RC mice (30.36 ± 0.85 g). *$P < 0.0277$; **$P < 0.0005$; ***$P < 0.0008$. (**H** and **I**) After treating mice with C1-BODIPY-C12

FFA for either 1 day (H) or 8 days (I), adipocytes but not LCs incorporate fluorescent FFA. Experimental timelines are shown at the top. FITC, fluorescein isothiocyanate. Scale bars: 100 μm [(A) to (D), bottom panels, and (H) and (I)]; 2 mm [(A) to (D), top panels].

To directly examine dietary lipid uptake, we injected mice with the fluorescently labeled fatty acid C1-BODIPY-C12. Six hours after a single injection in 1-month-old mice (n = 3) (Fig. 3H), C1-BODIPY-C12 substantially incorporated into perigonadal WAT (Fig. 4H, right) but was undetectable in ear lipocartilage (Fig. 4H, left). We also performed daily probe injections for 8 days starting at P10 (n = 3) (Fig. 4I) and observed that C1-BODIPY-C12 broadly incorporated into perigonadal WAT (Fig. 4I, right) as well as into adipocyte clusters within ear cartilage fenestrae but not into LCs (Fig. 4I, left). To examine lipid catabolism, we compared 1-month-old lipocartilage and WAT using fluorescence lifetime imaging microscopy (FLIM) at 740-nm excitation wavelength. This approach identifies endogenously fluorescent, long-lifetime molecular species (LLSs) that serve as a label-free marker of lipid catabolism and peroxidation (*22*). We saw a strong LLS signature (fig. S17C, red) that, when mapped back to the original images, localized to lipid vacuoles in perigonadal adipocytes (n = 4) (fig. S17D, red) and adipocytes within ear cartilage fenestrae (n = 5) (fig. S17F, red) but not in LCs (n = 5) (fig. S17E). Thus, in contrast to adipocytes, LCs have stable lipid vacuoles that are insensitive to fluctuations in dietary fat and are shielded from lipid catabolism. The gene expression signature of LCs, depleted of key fatty acid transporters and neutral lipid mobilization factors, was consistent with the observed biology.

LCs require de novo lipogenesis

Lack of dietary lipid uptake in LCs suggests that their vacuoles must rely on endogenous production of lipids from glucose through de novo lipogenesis. To directly test this assumption, we imaged the incorporation of glucose-derived deuterium into the lipid vacuoles of developing LCs using stimulated Raman scattering (SRS) microscopy. This approach detects vibrational properties of molecules, such as carbon-hydrogen (C-H) bonds in lipids (*23*). We cultured P14 mouse ears for 72 hours in high-glucose control media (n = 3) or in glucose-free media supplemented with deuterated glucose (G-d7) (n = 3). A strong carbon-deuterium (C-D) signal was detected in lipid vacuoles of G-d7–exposed LCs (Fig. 3, E and F) but not control LCs (fig. S17, A and B). In the Raman spectrum, the C-D signal observed in G-d7–exposed LCs matched the C-D signal profile of pure G-d7 (Fig. 3G, red region) and spatially overlapped with the strong C-H signal of LC lipid vacuoles, which indicated incorporation of deuterium into LC lipid stores (Fig. 3H). Considering that normal fasting blood glucose levels in mice are 80 to 100 mg/dl (equivalent to 4.4 to 5.5 mM), we also cultured microdissected P16 mouse ear lipocartilage in media containing either low (4 mM) or high (25 mM) concentrations of glucose. On BODIPY staining after 5 days, cultured lipocartilage showed significantly larger lipid droplets relative to culture day 0 (P < 0.0001), with lipocartilage cultured under high glucose (n = 4) also showing significantly larger lipid droplets relative to low glucose–exposed lipocartilage (n = 4) (P < 0.0001) (fig. S18).

Next, we disrupted de novo lipogenesis pathway in vivo. Starting at P10, we performed daily topical applications of acetyl–coenzyme A (CoA) carboxylase inhibitors PF-05175157 and ND-

646 (*24*, *25*) or C75, a FASN inhibitor (*26*), on mouse ears. By P21, in all three cases, we observed reduction in ear sizes (Fig. 3, I and K to N), with ND-646 and C75 inducing prominently misshapen ears that were 88 ± 2% (Fig. 3M) and 55 ± 7% smaller in size, respectively (Fig. 3N), compared with dimethyl sulfoxide (DMSO)–treated controls. On BODIPY staining, parts of the ear cartilage in C75-treated mice contained large areas devoid of lipid vacuoles (Fig. 3J). Thus, differentiating LCs grow lipid vacuoles through de novo lipogenesis from glucose.

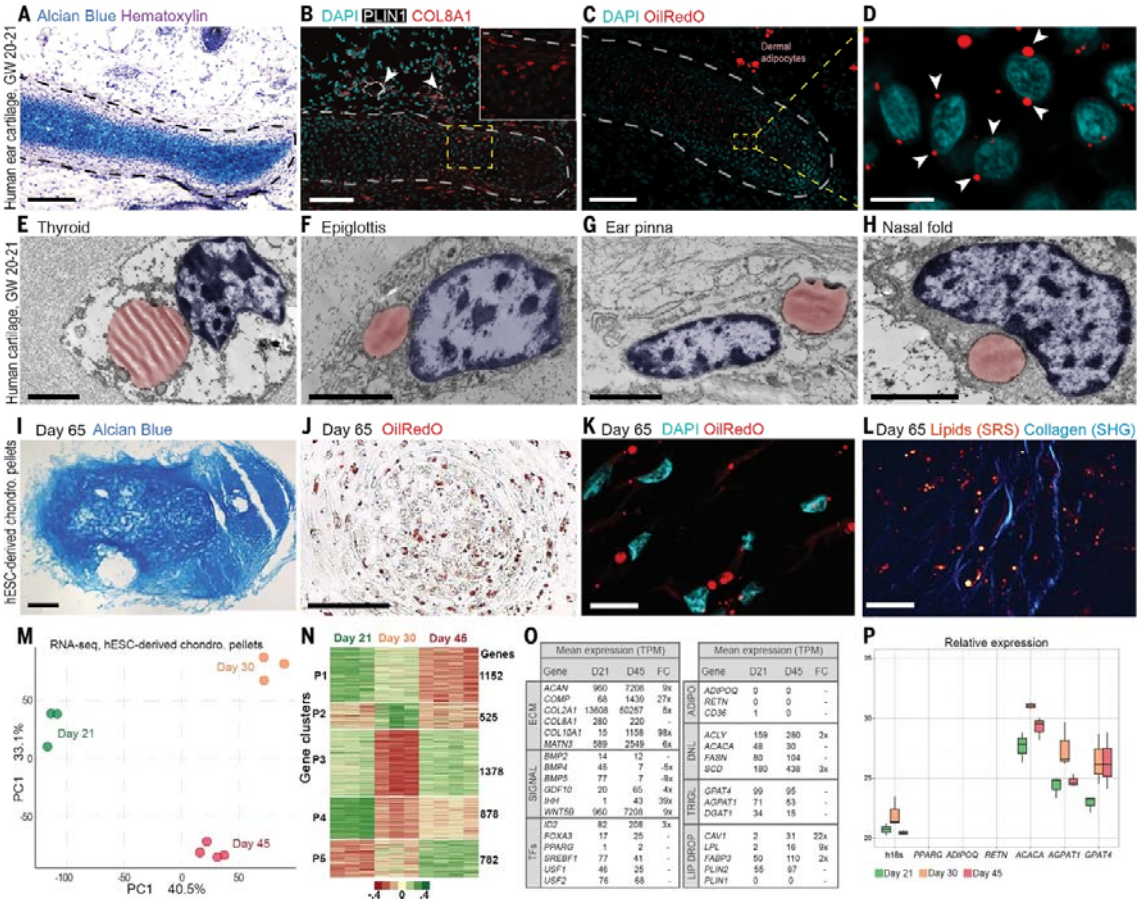

Fig. 5. Human head and neck cartilage accumulates lipid vacuoles.

(**A**) Alcian blue staining of human fetal ear cartilage at GW20 to GW21. (**B**) Immunostaining patterns of COL8A1 and PLIN1 in GW20 to GW21 human ear. Adipocyte marker PLIN1 is confined to dermal adipocytes and is absent in chondrocytes. (**C** and **D**) OilRedO staining pattern in GW20 to GW21 human ear. Numerous lipid vacuoles are present in chondrocytes. (**E** to **H**) Electron micrographs of GW20 to GW21 human thyroid cartilage (E), epiglottis (F), ear cartilage (G), and nasal cartilage fold (H) reveal chondrocytes with large lipid vacuoles. Nuclei and lipid vacuoles are pseudocolored purple and red, respectively. (**I**) Alcian blue staining of hESC-derived cartilage pellet at in vitro culture day 65. (**J** and **K**) OilRedO staining of day 65 pellets shows numerous lipid vacuoles in chondrocytes. (**L**) Label-free imaging of day 65 cartilage pellets reveals lipid vacuoles (SRS signal, red) and fibrillar collagen (second-harmonics generation signal, blue). (**M** and **N**) PCA and heatmap analyses show dynamic gene expression changes in hESC-derived cartilage pellet across three time points, days 21, 30, and 45. Across these time points, 4715 genes are differentially expressed (table S8). (**O**) List of selected genes within ECM, signaling, and transcription factor (TF) categories and their expression levels in hESC-

derived cartilage pellets at days 21 and 45. TPM, transcripts per million. (**P**) Relative expression values of hallmark adipogenesis and lipogenesis genes in hESC-derived pellets across days 21, 30, and 45 measured on qRT-PCR. Scale bars: 2 μm [(E) to (H)]; 10 μm (D); 15 μm (K); 25 μm (L); 50 μm (J); 100 μm [(A) to (C) and (I)].

LCs form in human cartilage

Next, we examined human fetal cartilage at gestational week (GW) 20 to 21. At this stage, ear cartilage had undergone maturation and strongly stained with sulfated glycosaminoglycan dye Alcian blue (Fig. 5A) and expressed collagen COL8A1 (Fig. 5B). Notably, this cartilage also contained numerous lipid vacuoles (Fig. 5, C and D), despite not expressing adipocyte-specific marker PLIN1 (Fig. 5B). Frequent and large lipid vacuoles were confirmed in ear, nasal, and thyroid and epiglottic GW20 to GW21 human cartilage by transmission electron microscopy (Fig. 5, E to H). Next, we studied cartilage organoids generated in vitro from a human embryonic stem cell (hESC)–derived neural crest intermediate (*27*). Similar to fetal ear cartilage, day-65 cartilage organoids strongly stained with Alcian blue (Fig. 5I) and contained numerous $OilRedO^{+}$ lipid vacuoles (Fig. 5, J and K). Lipid content of these vacuoles and the presence of a collagen-rich ECM was confirmed by SRS microscopy and second-harmonic generation, respectively (Fig. 5L).

To gain a molecular insight into human cartilage lipogenesis, we profiled hESC-derived cartilage organoids on RNA-seq at days 21 (n = 3), 30 (n = 3), and 45 of differentiation (n = 4). Day 21 was chosen as the starting point because organoids first become Alcian blue positive at this stage (*27*). On analysis, organoids prominently segregated by time point, with 4715 differentially expressed genes (Fig. 5, M and N, and table S8). Many of these genes paralleled the expression dynamics observed during mouse lipocartilage development (Fig. 3, B to D), including within ECM, signaling, transcription factor, and lipid biogenesis categories (Fig. 5O). Notably, analogous to mouse LCs, human organoids expressed lipogenic factor *SREBF1* but not *PPARG*. They also lacked expression of adipokines *ADIPOQ* and *RETN* or *CD36* and *PLIN1*, required for fatty acid uptake and mobilization, respectively. At the same time, similar to mouse LCs, they prominently expressed core de novo lipogenesis factors *ACLY*, *ACACA*, *FASN*, and *SCD*; triglyceride synthesis factors, including *GPAT4*, *AGPAT1*, and *DGAT1*; and lipid droplet biosynthesis genes, including *CAV1*, *LPL*, *FABP3*, and *PLIN2* (Fig. 5, O and P). Thus, lipid vacuole formation is an integral part of human craniofacial cartilage differentiation—a program that is recapitulated in hESC-derived cartilage organoids.

Lipocartilage is prevalent in mammals

Next, we examined whether lipocartilage exists in mammals from distinct phylogenetic groups. Owing to the ease of collection from preserved museum samples, we primarily focused our study on the external ear, a distinguishing feature of most extant mammals, with its earliest paleontological evidence dating to the Early Cretaceous, 125 million years ago (*28*). We examined ear cartilage from a total of 65 species, covering 4 orders of marsupials and 18 orders of eutherians, and found lipocartilage in multiple species across the clade (Fig. 6A and table S9) (*29*). We observed that prominent lipid-filled cells existed in the ear cartilage of

species with thin, membrane-like ears, irrespective of their phylogeny. However, ear lipocartilage morphology was diverse across species. In rodent species, such as spiny mice (*Acomys cahirinus*) (Fig. 6B) or jerboa (*Jaculus jaculus*) (Fig. 6C), lipocartilage generally resembled that of *Mus musculus*—a flat plate of tightly packed LCs with fenestrae, some of which contain adipocyte clusters. Notably, we also saw fenestrated lipocartilage in marsupial species, where, in addition to adipocytes, fenestrae could contain pigmented material, as seen in kowari (*Dasyuroides byrnei*) (Fig. 6D) or opossum (*Didelphis virginiana*) (fig. S19A). In other marsupials, such as the squirrel glider (*Petaurus norfolcensis*) (Fig. 6E), many of the fenestrations nestled hair follicles, one per opening. In bat species, such as in Pallas's long-tongued bat (*Glossophaga soricina*) (Fig 6F), LCs differentially distributed across lipocartilage—sparsely along the medial side and in the shape of periodic parallel ridges along the lateral side. Ridges consisted of "stacks" of lipid-laden cells and gave the ear a "ruffled" morphology, important for sound perception (*30*). Other bat and rodent species also showed clear LCs in nasal cartilage (fig. S19, B to D). Prominent lipid vacuoles were also found in the ear cartilage of some Afrotherians, such as the eastern rock elephant shrew (*Elephantulus myurus*) (Fig. 6G).

Finally, we inquired about the presence of lipocartilage in nonmammalian tetrapods. We performed Alcian blue and OilRedO staining on tracheal and peri-tracheal cartilages from two amphibians, Forrer's grass frog (*Lithobates forreri*) and axolotl (*Ambystoma mexicanum*) (fig. S20); a chicken (*Gallus gallus*) (fig. S21); and three reptilians, the American alligator (*Alligator mississippiensis*), green anole (*Anolis carolinensis*), and red-eared slider turtle (*Trachemys scripta elegans*) (fig. S22). In all instances, cartilage did not contain lipid droplets and, instead, had the morphology of canonical ECM-rich hyaline cartilage. We therefore posit that lipid-filled cells are a common feature of cartilage across the mammalian clade exclusively and are not found in other tetrapods.

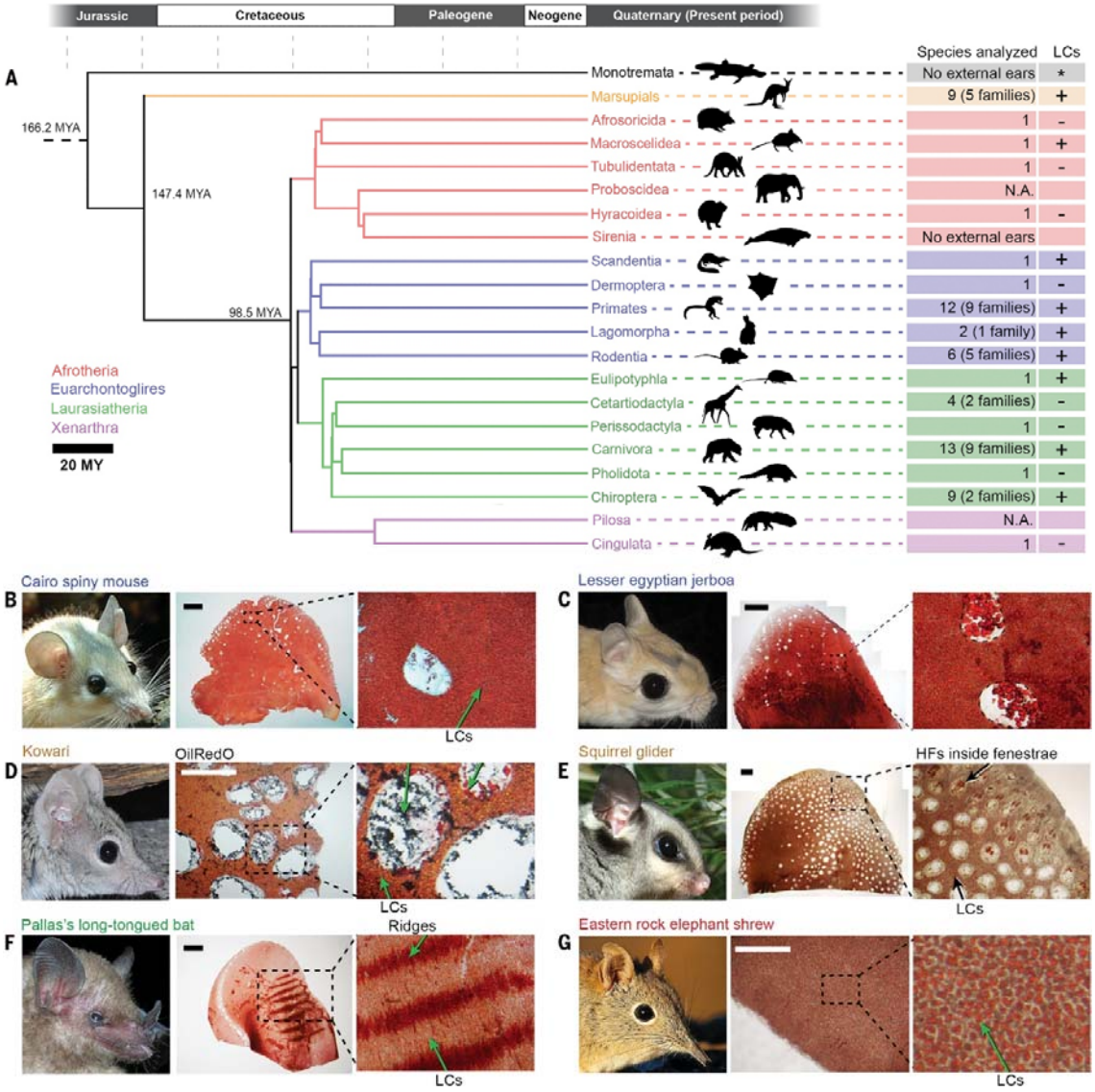

Fig. 6. Lipocartilage is a prevalent feature of mammals.

(**A**) Phylogenetic tree of extant mammalian clades, with branches representing monotremes (black), marsupials (yellow), and placentals, further separated by order (different colors indicate superorders). The table on the right provides information on the number of species for which ear cartilage was analyzed within each taxon and whether OilRedO$^+$ LCs were detected (table S9). MY, million years; MYA, million years ago; N.A., not applicable. (**B** and **C**) Representative examples of ear lipocartilage in rodents: *A. cahirinus* (Cairo spiny mouse) (B) and *J. jaculus* (lesser Egyptian jerboa) (C). (**D** to **G**) Representative examples of ear lipocartilage in nonrodent mammals: *D. byrnei* (kowari; marsupial) (D), *P. norfolcensis* (squirrel glider; marsupial) (E), *G. soricina* (Pallas's long-tongued bat; order Chiroptera) (F), and *E. myurus* (eastern rock elephant shrew; superorder Afrotheria) (G). Cartilage fenestrae and fenestra-associated adipocytes are evident in many species. Squirrel glider ear cartilage (E) shows fenestra-associated hair follicles (HFs). Pallas's long-tongued bat ear cartilage (F) shows complex distribution of LCs, with sparse LCs along the medial side and ridgelike LC "stacks" along the lateral side. Scale bars: 20 million years (A); 1 mm [(D) and (G)]; 2 mm [(B), (C), (E), and (G)].

Discussion

In this work, we have shown that LCs are not adipocytes but are instead a type of lipid-filled skeletal cell. Although our experiments have defined some of the essential properties of LCs, such as their longevity, size stability, gene expression, and lipid biochemistry, many other aspects of their biology remain unexplored.

A key and distinctive property of LCs that emerged from our work is their ability to form superstable lipid vacuoles. Unlike adipocytes, LCs maintain stable lipid vacuoles upon maximal obesity as well as acute starvation. LCs manage to "untether" from systemic metabolism by not expressing fatty acid transporters and other key lipid-mobilization factors. In-depth studies will be needed to determine the transcriptional and epigenetic regulations of lipid pathways in LCs. The longevity of LCs and their ability to tolerate high content of otherwise cytotoxic lipids present an opportunity to use them in studying mechanisms of cellular aging. Additionally, the uniformity and extreme stability of LCs' lipid vacuoles hold clues to the mechanism of cell size control.

Enlargement of LCs through lipid droplets is a form of cellular hypertrophy. Differentiating chondrocytes in hyaline cartilage poised for ossification also undergo hypertrophy through cytoplasmic swelling. However, molecular aspects of the hypertrophy program in LCs are distinct from those in hyaline chondrocytes, and unlike hyaline cartilage, lipocartilage is not a template for ossification but rather a permanent lipid-filled skeletal structure. Lipid droplets can accumulate in chondrocytes within joints upon obesity, contributing to osteoarthritis (*31*). However, unlike in LCs, such lipid-laden articular chondrocytes are diseased—they display dysregulated metabolism and aberrant gene expression, furthering osteoarthritis pathogenesis (*32*). Studying how lipid-filled LCs maintain a healthy cell state relative to diseased lipid–filled articular chondrocytes can offer molecular interventions strategies for osteoarthritis.

Our study elucidates structure-function relationships in skeletal tissues. Key mechanical properties of cartilage—stiffness and strength—have been attributed to their ECM composition and organization (*33*, *34*). Our findings show that lipocartilage displays robust mechanical properties despite consisting of giant lipid-filled cells with minimal ECM, which suggests that key paradigms in tissue biomechanics should be reconsidered. Currently, cartilage biomechanics are commonly described using continuum theory, assuming that ECM is homogeneous and that mechanical contribution from cells is negligible (*35*, *36*). Lipocartilage biomechanics may require theories that consider the discontinuous and heterogeneous structure of the tissue as well as the compliance offered by the lipid vacuoles.

Lipocartilage in many species has intricate morphology, with that in bat ears being particularly complex, featuring arrays of parallel and interconnected microridges thought to be essential for proper sound perception. We show that such microridges result from the precise stacking of individual LCs. In-depth studies will be needed to determine the nature of morphogenetic mechanisms that precisely reposition large lipid-filled cells into intricate microshapes.

We propose that lipocartilage is an outcome of convergent evolution and is analogous to the notochord. The latter is an ancient skeletal tissue type that first appeared in early Chordates and that, in extant mammals, forms the nucleus pulposus of the intervertebral discs (*37*). A key morphological feature of the notochord and its derivatives is their giant, tightly packed vacuolated cells. However, unlike the LCs in lipocartilage, cells of the notochord contain aqueous rather than lipid vacuoles. Biomechanical properties of the notochord are determined by virtue of hydrostatic forces generated between its vacuolated cells (*38*). As supported by delipification experiments, the biomechanical properties of lipocartilage arise, at least in part, from the "lipo-elasticity" of LCs.

We also propose that the high and molecularly distinct lipid content of ear lipocartilage may aid in the ear pinna's ability to gather and focus acoustic waves—an essential process in mammalian sound perception. In fact, animals are shown to use lipid-rich tissues in bioacoustics.

Abundant lipid vacuoles form in neural crest–derived cartilage organoids induced in vitro from hESCs. We propose that lipid vacuoles can be used as a biomarker for the purification of differentiated human cartilage cells in hESC-derived cultures. A major hurdle for using hESC-derived cells in regenerative medicine is the inability to reliably separate differentiated cells from pluripotent progenitors, which presents a risk for teratoma development. Lipid vacuoles can be labeled easily and reliably with intravital fluorescent lipid dyes, and labeled differentiated chondrocytes can be purified by fluorescence-activated cell sorting (FACS). Application of lipid vacuole–based cell purification to hESC- or induced pluripotent stem cell (iPSC)–derived cartilage organoids could potentially help advance regenerative approaches to cartilage repairs.

In this study, we characterized a distinct type of lipid-rich skeletal tissue present in many mammals. This tissue develops from embryonic progenitors that first acquire a chondrogenic cell fate but then proceed to differentiate by synthesizing giant lipid vacuoles—a distinct mechanism from that of conventional cartilage. We showed that the resulting lipid vacuoles are superstable and do not contribute to systemic lipid metabolism but, instead, confer the tissue with its biomechanical properties. Our observations lay a foundation for studies on the nonmetabolic roles of lipid vacuoles in skeletal tissue morphogenesis, homeostasis, and function.

Materials and methods

Experimental mouse models

Wnt1-Cre2 (JAX, no. 022137), *mT/mG* (JAX, no. 007576), *R26R* (JAX, no. 003309), *tdTomato* (JAX, no. 007914), *Col2a1-CreER^{T2}* (JAX, no. 006774), *Retn-lacZ* (*39*), *Adipoq-Cre* (JAX, no. 010803), *db/db* (JAX, no. 000697), and *C57BL/6J* DIO (JAX, no. 380050) were used. In *Col2a1-CreER^{T2};R26R* mice, tamoxifen in corn oil was injected intraperitoneally (IP) for 4 consecutive days starting at P21 at a dose of 75 mg/Kg for full induction. For low-dose induction, a single dose of tamoxifen in corn oil at 7.5 mg/Kg was injected IP at P6. All animal experiments were approved by the Animal Care and Use Committee of National Taiwan University (to S.-J.L.)

and/or the Animal Care and Use Committee of National Cheng Kung University (to C.-C.Y.) and/or the Institutional Animal Care and Use Committee at University of California, Irvine (to M.V.P.) and/or the Institutional Animal Care and Use Committee at Kyungpook National University (to J.W.O.).

Lipidomic and proteomic profiling

All lipid standards were acquired from Cayman Chemical Company, Matreya, Cambridge Isotope Laboratories, NuChek Prep, Avanti Polar Lipid, or Sigma-Aldrich. All solvents were of high-performance liquid chromatography (HPLC) or liquid chromatography–mass spectrometry (LC-MS) grade and were acquired from Sigma-Aldrich, Fisher Scientific, or VWR. Medial, fenestrae-free zones of the ear cartilage plate were dissected from adult P33 C57Bl/6J female mice (at least 10 mg per sample), carefully avoiding adipocytes. For WAT control, inguinal fat was collected (at least 10 mg per sample). All tissues were rinsed thoroughly in 1X phosphate-buffered saline (PBS) and flash frozen for downstream use.

For lipidomic analysis, tissues were thawed in 10 times diluted PBS and homogenized in Omni bead tubes with 2.8-mm ceramic beads in the Omni Bead Ruptor 24 with Cryo Cooling Unit (Omni International) at 4°C for 2 min. Protein concentration was determined by the bicinchoninic acid assay. 1 mg of protein from each sample was aliquoted, and a cocktail of deuterium-labeled and odd chain phospholipid standards from diverse lipid classes was added. Standards were chosen so that they represented each lipid class and were at designated concentrations chosen to provide the most accurate quantitation and dynamic range for each lipid species. 4 ml chloroform:methanol (1:1, by volume) was added to each sample, and lipidomic extractions were performed. Lipid extraction was automated using a customized sequence on a Hamilton Robotics STARlet system (Hamilton). Lipid extracts were dried under nitrogen and reconstituted in chloroform:methanol (1:1, by volume). Samples were flushed with nitrogen.

Samples were diluted 50 times in isopropanol:methanol:acetonitrile:water (3:3:3:1, by volume) with 2 mM ammonium acetate to optimize ionization efficiency in positive and negative modes. Electrospray ionization–mass spectrometry was performed on a TripleTOF 5600+ (SCIEX), coupled to a customized direct injection loop on an Ekspert microLC200 system (SCIEX). 50 ml of sample was injected at a flow rate of 6 ml/min. Lipids were analyzed using a customized data-independent analysis strategy on the TripleTOF 5600+ allowing for MS/MSALL high-resolution and high–mass accuracy analysis. Quantification was performed using an in-house library on MultiQuant software (SCIEX) and normalized to 1 mg of protein.

For proteomic analysis, tissues were digested in mass spectrometry grade trypsin at 65°C overnight to form a complete, homogeneous peptide digest. Digests were desalted using C18 cartridges (Waters Sep-Pak) per manufacturer's protocol, concentrated under vacuum, and resuspended in 0.1% formic acid. Peptides underwent bottom-up proteomics analysis with label-free quantification (LFQ). Briefly, samples were injected into a Thermo Fischer Scientific UltiMate 3000 RSLC system coupled to a Thermo Fischer Scientific Orbitrap Fusion Lumos mass spectrometer at a flow rate of 300 nl/min. Identification and LFQ were performed using

MaxQuant software. Resulting LFQ values were used for comparing the relative abundance of proteins among different samples, normalized to total protein content.

Tissue delipification for mechanical testing

Adult rat ear cartilage tissue was dissected and rinsed in fresh 1X PBS. Using a tissue biopsy punch, 6-mm-diameter discs were prepared and either left intact as native tissue controls or processed through a methanol gradient in 1-hour 25% increments until absolute methanol. Samples were then incubated twice in fresh absolute methanol for a minimum of 15 min, then transferred into a 2:1 chloroform-methanol solution for 3 hours in a rocking platform, then taken through a reverse methanol gradient into 1X PBS and rinsed at least three times before downstream analysis.

Mechanical testing and analysis

For mechanical testing, uniaxial tensile tests were performed. Briefly, tissues are dissected and rinsed in cold 1X PBS. Note that for delipification studies, control and delipified tissues were generated as described in the previous subsection. Tissues are then cut into bone-shaped pieces and imaged to obtain dimensions using ImageJ analysis. Samples were paper tabs, loaded into an Instron Model 5565, and pulled to failure at a rate of 1% strain per second. Force-displacement curves were used to calculate tensile Young's modulus, UTS, and ultimate tensile strain using a custom MathWorks' MATLAB code, as previously described (*40*).

Histology and immunostaining

For hematoxylin and eosin (H&E) staining, paraformaldehyde (PFA)–fixed sections were immersed in Harris' H&E solutions (National Diagnostics) following the manufacturer's suggestions, dehydrated, cleared, and mounted in toluene. For lacZ staining, tissues were fixed in 4% PFA for 30 min at room temperature, rinsed in 1X PBS and incubated in lacZ buffer at 37°C for 5 min, then transferred to lacZ buffer with X-Gal (VWR) and incubated at 37°C until signal developed. For OilRedO (VWR AMRESCO) staining, a 6.25 mg/ml stock solution in isopropanol was prepared and diluted as a working solution to 60% in H_2O followed by filtration immediately before staining. Tissues were fixed in 4% PFA for 8 hours at 4°C, rinsed twice in H_2O, then submerged in 60% isopropanol for 1 min followed by staining in OilRedO working solution for 30 min. Tissues were then rinsed twice in 60% isopropanol followed by H_2O and imaged in 1X PBS. For BODIPY staining, tissues were incubated in 200 μM BODIPY 493/503 (Thermo Fisher) in 1X PBS for 30 min, rinsed twice in 1X PBS and imaged. For Alcian blue staining, fixed tissue sections were immersed in 1% Alcian blue 8GX in 3% aqueous acetic acid (pH 2.5) for 30 min, rinsed in distilled water, and, for fetal ear, counterstained with Harris hematoxylin before procedural dehydration and mounting. The primary antibodies used were rabbit anti-COL8A1 (1:500; Antibodies-Online), rat anti-CD31 (1:250; Invitrogen), mouse anti-MYOC (1:250; ProteinTech), rabbit anti-FASN (1:250; Cell Signaling Technology), rabbit anti-PLIN1 (1:750; Cell Signaling Technology), rabbit anti-SOX9 (1:250; Millipore), and mouse anti-PCNA (1:200; Abcam). Secondary antibodies used were Alexa Fluor 488 and 555 goat anti-

rabbit (ThermoFisher) and goat anti-mouse (ThermoFisher) at 1:1000. Stained sections were mounted with nonhardening mounting medium with 4',6-diamidino-2-phenylindole (DAPI) (Vector Laboratories). For mouse anti-PCNA and rabbit anti-SOX9, immunostaining was performed on paraffin sections with heat-based antigen retrieval; for other antibodies frozen tissue sections were used.

RNAscope in situ assay

Mouse ear pinna tissue sections were used for RNA in situ hybridization using RNAscope kit v2 (323100, Advanced Cell Diagnostics), following the manufacturer's instructions. The following *M. musculus* probes from Advanced Cell Diagnostics were used: *Mm-Col8a1* (51807), *Mm-Fasn-C2* (490661-C2), *Mm-Acaca-C2* (576581-C2), *Mm-Dgat2-C2* (481301-C2), *Mm-Cd36-C2* (464431-C2), *Mm-Acly-C2* (460391-C2), and *Mm-Sox9-C3* (401051-C3).

RNA extraction and RNA-seq

Mouse ear cartilage tissues were collected from *Wnt1-Cre2;tdTomato* mice at several postnatal time points. In P8, P10, and P13 mice, red fluorescence–positive ear cartilage was microdissected and incubated in 0.75 mg/ml Collagenase I (Sigma-Aldrich) in 10% fetal bovine serum (FBS) Dulbecco's minimum essential medium (DMEM) for 3 hours at 37°C in 5% CO_2 with constant motion. The cell suspension was passed through a 40-μm nylon cell strainer (Corning) and centrifuged at 1200 rpm. The cell pellet was reconstituted in 1X PBS and stained with Zombie Violet Cell Viability Kit (BioLegend) according to the manufacturer's protocol. Single, live-cell fractions were then FACS-sorted as tdTomato^{hi} using a BD FACSAria II flow cytometer (BD Biosciences). In P21 and P33 mice, the ear cartilage plate was microdissected, and the medial and distal portions of the plate were separated and incubated in Collagenase I. Dissected inguinal adipose tissue was also treated to isolate single adipocytes. Cells were passed through a 100-μm nylon cell strainer (Corning) and centrifuged at 1200 rpm. After centrifugation, the buoyant, lipid-filled cell fraction was collected. Sorted tdTomato^{hi} cells (from P8, P10, and P13) and buoyant cells (from P21 and P33) were resuspended in RLT buffer (QIAGEN) with 1% beta-mercaptoethanol and homogenized. Similarly, hESC-derived cartilage pellets were collected at differentiation days 21, 30, and 45, rinsed three times in 1X sterile PBS, and homogenized in RLT buffer with 1% beta-mercaptoethanol. Total RNA was isolated using the RNEasy Micro-Kit (Qiagen). Optimal-quality RNAs with RNA integrity number (RIN) scores more than 8.8 were considered for cDNA library preparation. Full-length cDNA library amplification was performed as previously described (*41*) with minor modifications. Briefly, 1 ng of total RNA was reversed-transcribed, and resulting cDNA was preamplified for 13 cycles. Tagmentation was carried out on 18 ng of cDNA using the Nextera DNA Sample Preparation Kit (Illumina) at 55°C for 5 min and purified using PCR Purification Kit (Qiagen). Transposed cDNA was used for limited cycle enrichment PCR using previously published Nextera PCR primers (*42*). Libraries were amplified for seven continuous cycles and purified with AMPure XP beads (Beckman Coulter). Library quantification was done using KAPA for Illumina Sequencing Platforms (Illumina). Libraries were multiplexed and sequenced as paired-end on an Illumina Next-Seq500 platform (cluster density = 296,000 per mm^2, clusters passing filter

= 71.2%, Q30 = 87.6%). The libraries were sequenced to an average depth of 10 to 30 million reads per library using paired 43–base pair reads.

Gene expression analysis

Reads were first aligned using STAR v.2.4.2a with parameters "--outFilterMismatchNmax 10 --outFilterMismatchNoverReadLmax 0.07 --outFilterMultimapNmax 10" to the reference mouse genome (mm10/genocode,vM8), or, in the case of hESC-derived cartilage pellets, aligned to the reference human genome (GRCh38). Gene expression levels were quantified using RSEM v.1.2.25 with expression values normalized into fragments per kilobase of transcript per million mapped reads (FPKM). Samples with >1,000,000 uniquely mapped reads and >60% uniquely mapping efficiency were used for downstream analyses. Differential expression analysis was performed using edgeR v.3.2.2 on protein-coding genes and lncRNAs. Differentially expressed genes were selected by using fold change (FC) ≥ 2, false discovery rate (FDR) < 0.05, and counts per million reads (CPM) ≥ 2.

On analysis, numerous genes encoding secreted signals and transcriptional regulators were differentially expressed between LCs and rib chondrocytes. In terms of secreted signals, both cartilage cell types expressed BMP ligands, but LCs were enriched for *Bmp5*, whereas rib chondrocytes were enriched for *Bmp4/6/7/8a*. Among TGFβ ligands, LCs express *Gdf5* and *Tgfb3*, whereas rib chondrocytes expressed *Gdf10/15* and *Tgfb1*. In terms of the WNT pathway, LCs were enriched for WNT antagonists *Dkk3*, *Sfrp1/2/5*, and *Wif1*, whereas rib chondrocytes were enriched for WNT ligands *Wnt5a/5b/10b/11*. Rib chondrocytes also prominently expressed *Ihh*, *Spp1*, *Tnf*, *Vegfa*, and a large number of chemokines *Ccl2/3/4/5/7/8/9/12/24*, *Cxcl1/2/3/10/16*, and interleukins *Il1b/1f9/17b/17d*. Other secreted signals specifically enriched in LCs include angiopoietins *Angpt4*, *Angptl7*, FGF ligands *Fgf7* and *Fgf18*, IGF binding proteins *Igfbp2/4/5/6/7*, and cytokine-like protein *Cytl1* (table S3).

LCs and rib chondrocytes showed distinct expression patterns for transcriptional regulators, including homeobox and homeobox-like genes. Reflecting their thoracic origin, rib chondrocytes were enriched for *Hoxa3/5/6/7*, *Hoxb2/7*, and *Hoxc5/6/8*. In a similar fashion, ear LCs were enriched for *Hoxa2*, *Dlx5/6*, and *Msx1*, reflecting their origin from neural crest mesenchyme of the second pharyngeal arch (*43*). Both cartilage cell types shared expression of known chondrogenic regulators, including *Id2*, *Smad4*, *Snai1/2*, *Sox5/6/8/9*, and *Twist1*. At the same time, only rib chondrocytes expressed high levels of the following established regulators of chondrogenesis: *Foxa3*, *Foxo4*, *Nkx3-2*, *Runx1/3*, *Smad7*, *Sox4*, *Sp7*, and *Vdr*. LCs specifically expressed *Cbx6*, *Foxn3*, *Glis2/3*, *Lhx8*, *Mkx*, *Scx*, and *Tbx15*. Notably, they also expressed several known transcriptional regulators of adipogenesis: *Cebpa*, *Klf9*, *Nfia*, *Pparg*, *Srebf1*, and *Zfp423*, albeit at lower levels than adipocytes (table S3).

Spatial transcriptomic data analysis

We examined recently published high-resolution spatial sequencing data (Stereo-seq technology) collected on sagittal sections cut through the whole mouse embryo at developmental stage E16.5 (*44*). Specifically, we analyzed the "E16.5_E2S5.MOSTA" sample,

which was downloaded from https://db.cngb.org/stomics/mosta/download/ because it was significantly enriched for cartilage markers in the head regions. In the original study, spot counts were normalized to the median of total counts across all spots and then log-transformed, adding a pseudocount of 1. We analyzed the head and tail regions separately. First, we extracted the *x* coordinates and *y* coordinates of the spatial spots from the entire tissue, which we denote as *X* and *Y*, respectively. We reflected

to orient the tissue section in the correct direction when plotting *X* and *Y* directly. To isolate cartilage spots in the head or tail, we filtered for spots that were annotated in the original study as either "cartilage" or "cartilage primordium" and whose coordinates satisfied $X < -200$ and $-314 < Y < -255$ (head cartilage) or $X < -340$ and $Y < -500$ (tail cartilage). We then translated the spots from the tail region in the positive vertical direction so that they were closer to the spots from the head region. We reannotated the subsetted tissue as follows. Spots from the tail region that were originally annotated as "cartilage" were reannotated as "tail." Spots from the head region that were originally annotated as "cartilage primordium" were reannotated as "nasal cavity." Spots from the head region that were originally annotated as "cartilage" and whose locations satisfied $Y > -350$ (to avoid the tail cartilage) and $Y < -1.915(X + 370)$ were reannotated as "nasal." All other spots from the head region that were originally annotated as "cartilage" were reannotated as "palate."

For qRT-PCR, cDNA from hESC-derived cartilage pellets was generated from RNA extracted as indicated above using Reverse Transcriptase II cDNA synthesis kit (Invitrogen) and Oligo(dt)20 primer (ThermoFisher). qRT-PCR was performed on a QuantStudio7 instument (ThermoFisher) using manufacturer's recommendations (for primers, see table S10).

Modified diet experiments

Male C57BL/6J mice were fed ad libitum with a high-fat chow (for 39 weeks, starting at P21) or placed under caloric restriction for 72 hours with water only starting at P33. Control mice were fed ad libitum with normal chow for 39 weeks starting at P21. The obesity model mice *C57BL/6J* DIO were purchased from JAX at 16 weeks of age after 12 weeks of high-fat diet.

Fluorescent free fatty acid incorporation

One hundred microliters of 20 μM C1-BODIPY-C12 were injected peritoneally. Adult 1-month-old mice received single injection and were chased for 6 hours. P10 mice received daily injections at 24-hour interval for 8 days and were chased for 6 hours after the last injection.

Histological measurements

Cell area and ear pinna area was measured in ImageJ using the polygon selection tool and the "Measure" function. Ear pinna area measurements were standardized using natural ear landmarks (apex of the antihelix) for all samples. Lipid droplet area was measured using the MRI_Lipid Droplet Tool.

Topical drug treatment

C75 (Cayman Chemical), ND-646 (MedChemExpress), and PF 05175157 (TOCRIS) were dissolved individually in DMSO at 40 mM, 5 mM, and 50 mM concentrations, respectively. 20 µl of either drug was painted on the ears of wild-type mice for 10 consecutive days, starting at P11. Changes to ear morphology were monitored daily, and final size was measured on day 10 of treatment, at P21. Control mice received topical treatment of DMSO vehicle only (VWR).

Glucose modulation experiments

Culture media was prepared with glucose-free DMEM, 10% FBS (ThermoFisher), and 1X PenStrep. Media was supplemented with either low (4 mM) or high (25 mM) glucose (Gibco). Day P16 mouse ears were microdissected by removing both caudal and rostral skin flap and trimming away excess muscle tissue from the cartilage and rinsing in fresh 1X PBS. Tissues were then cultured for 5 days in low or high glucose conditions. Media was replaced every 48 hours. Tissues were cultured at 37°C in 5% CO_2, 5% O_2 throughout the procedure.

Glucose-d7 ex vivo ear culture

P14 ears were partially dissected by removing the caudal skin flap and exposing the cartilage, then cultured in media supplemented with glucose-d7. Briefly, glucose-d7–containing media was prepared with glucose-free DMEM (ThermoFisher Scientific), 25 mM glucose-d7 (Cambridge Isotope Laboratories), 10% FBS (Atlanta Biologicals), and 1X PenStrep. Tissues were cultured for 72 hours. Control samples were cultured for 72 hours in high glucose (25 mM) DMEM, 10% FBS, 1X PenStrep without glucose-d7 added. Media was replaced every 24 hours. All samples were rinsed with 1X PBS twice for 5 min and fixed with 4% PFA for 1 hour and imaged. Tissues were cultured at 37°C in 5% CO_2, 5% O_2 throughout the procedure.

hESC-derived cartilage pellet generation

hESCs were differentiated into neural crest intermediates and then terminally into cartilage pellets. Briefly, human embryonic stem cells line H1 (WA01) (WiCell Research Institute, Inc) was maintained in mTeSR 1 (Stem Cell Technologies) on matrigel coated dishes at 37°C in 5% CO_2, 5% O_2 and passaged regularly. For hNC differentiation, cells were collected 5 days after the last passage at ~80 to 90% confluency. Cells were first rinsed three times in 1X Ca+ and Mg + free PBS, then dissociated in Accutase (Stem Cell Technologies) for 4 min 30 s at 37°C in 5% CO_2, 5% O_2. Accutase was immediately quenched with warmed 1X DMEM/F12 (Invitrogen) containing 10 µM Rock Inhibitor, Y-27632 (Tocris), then centrifuged 1200 rpm for 4 min at room temperature. Media was discarded without disturbing cell pellets and replaced with NC Induction media [1X DMEM/F12 (Invitrogen), 1X serum-free B27 supplement (Invitrogen), 1X Glutamax (ThermoFisherScientific), 0.5% BSA (Sigma)] containing 10 µM Y-27632. hESC pellets were further dissociated to single cells mechanically through a 5-ml serological pipette. CHIR99021 (Tocris) was added to pellets in induction media during dissociation to a final concentration of 3 µM. Cells were counted and diluted to an optimal seeding density of 20×10^3 cells/cm^2 per vessel, then seeded on hESC-qualified Matrigel (BD) precoated vessels.

10 µM Rock Inhibitor, Y-27632, was added from days 0 to 2, then left out of induction media during the remainder of culture. Induction media was changed daily until day 5, when terminal differentiation began. For terminal differentiation into cartilage pellets, hESC-derived NC intermediates were centrifuged as described above to generate cell pellets. Pellets were carefully rinsed and left intact, and media was replaced with Mesencult-Chondrogenic Differentiation media (Stem cell technologies). At terminal differentiation day 21, pellets were gently dislodged from the bottom of the tube but not dissociated. Media was replaced every 2 to 3 days until collection for analysis. Cells were cultured at 37°C in 5% CO_2, 5% O_2 throughout the procedure. All experiments on hESCs were approved by the Stem Cell Research Oversight Committee (SCRO) at University of California, Riverside (to M.I.G.-C.) and SCRO at University of California, Irvine (to M.V.P.).

SRS microscopy

Ex vivo cultured ears were imaged through SRS to visualize lipid content and track deuterium incorporation into lipid droplets. Stimulated Raman loss was measured using a combination of a fixed stokes beam at 1064 nm generated by a 76-MHZ mode-locked Nd:Vanadate laser (Picotrain, High-Q) delivering 7-ps pulses and a variable pump beam generated through an optical parametric oscillator (OPO, Levante Emerald, APE) pumped by the second harmonic of the laser at 532 nm. For imaging of the CH2 lipid mode, the OPO was tuned to 817 nm and for deuterated imaging it was tuned to 868 nm. For stimulated Raman loss, the stokes beam was modulated at 10 MHz using an acousto-optic modulator (AOM) (Crystal Technology). After modulation, the two beams were combined and directed into a laser scanning inverted microscope (Fluoview 300 and IX71, Olympus). The SRS signal was collected on an output channel of the lock-in by the synced Fluoview system to form the intensity image. Additionally, linear Raman spectra were acquired for the P14 ear samples cultured for 72 hours and for pure standards using a confocal Raman microscope (InVia Confocal, Renishaw).

FLIM

Adult 1-month-old mouse ear cartilage plates were microdissected, rinsed in 1X PBS, and mounted in microscope slides. Inguinal adipose tissue was rinsed in 1X PBS, cut into 5-mm squares, and mounted. All dissections were performed within 1 hour of imaging. All FLIM data acquisition and processing were performed with software developed at the Laboratory of Fluorescence Dynamics (University of California, Irvine).

Electron microscopy

Human fetal tissue samples (ear and nasal septum cartilage, GW20 to GW21) were fixed in 10% phosphate buffered (pH 7.2 to 7.4) formalin for 2 to 3 days at room temperature, and 1.5-mm^2 pieces were cut out from each sample. Samples were subjected to three 10 min washes in 0.1 M Millonig's phosphate buffer and fixed by immersion in 1% osmium tetroxide fixative (Sigma-Aldrich) in 0.1 M Millonig's phosphate buffer (pH 7.4) containing 5.4% glucose at 4°C for 1 hour, dehydrated in graded dilutions of ethanol, followed by an ethanol-acetone mixture and, lastly, through three steps of acetone before embedding in Araldite. Sections

were cut with a Leica EM UC7 ultramicrotome using glass knives and mounted on formvar-film–coated copper grids. Thin sections from preselected areas were stained by immersion in a saturated solution of uranyl acetate and lead citrate Sections were examined with a JEM-1011 electron microscope at various magnifications.

Super-resolution microscopy

Structured illumination microscopy (also known as super-resolution) images were taken using an Elyra 7 (Zeiss) with a Plan-Apochromat 63x/1.4 Oil DIC M27 objective.

Acknowledgments

We thank R. Diaz, P. Wu, C.-M. Chuong, and J. M. Daglian for their help collecting animal tissue samples. We thank M. A. Lazar for providing the *Retn-lacZ* mouse line.

Funding: M.V.P. and K.A.A. are supported by W. M. Keck Foundation grant WMKF-5634988. M.V.P. is additionally supported by UCI Beall Applied Innovation's Proof of Product (PoP) grant IR-PR57179; LEO Foundation grants LF-AW-RAM-19-400008 and LF-OC-20-000611; Chan Zuckerberg Initiative grant AN-0000000062; Horizon Europe grant 101137006; NSF grants DMS1951144 and IOS-2421118; and NIH grants U01-AR073159, R01-AR079470, R01-AR079150, R21-AR078939, and P30-AR075047. K.A.A. is additionally supported by NIH grants R01-AR078389-01, R01-DE015038, R01-AR071457, and R01-AR067821. Q.N. is supported by NIH grants R01GM152494 and R01DE030565, NSF grants DMS1763272 and CBET2134916, and Simons Foundation grant 594598. R.C.N. is supported by NIH grant TL1-TR001415. K.Y. is supported by the Yoshida Scholarship Foundation. C.F.G.-J. is supported by the NSF-GRFP (DGE-1321846), a MBRS-IMSD training grant (GM055246), and a Howard Scheidermann Fellowship Award. T.F.S. is supported by NIH grants R01-DE013828, R01-DE30565, R01-HD073182, and R01-AR067797 and NSF grant MCB 2028424. M.I.G.-C. is supported by NIH grant R01-DE017914. R.R.B. is supported by the Ben F. Love Chair in Cancer Research. M.S.P. is supported by the UC Riverside School of Medicine Dean's Postdoc to Faculty fellowship. C.K.V. is supported by the Danish Cancer Society.

Author contributions: R.R. and M.V.P. conceptualized the research and wrote the paper. R.R., K.T.P., R.C.P., M.S.P., X.W., R.C.N., B.J.B., K.Y., R.D., A.A., J.T.B., Y.L., B.Q.T., Y.-L.C., A.M.N., T.-C.H., R.L., Y.-L.P., and C.K.V. performed experiments. R.R., R.C.N., B.J.B., T.P., A.A.Al., M.A.K., and M.V.P. curated data. L.B.L.-M., K.L.H., N.T.-L.L., S.S., A.E.Mc., F.v.B., M.K., W.J.L., S.H.W., R.C., C.-C.Y., K.L.C., S.E.S., J.E.B., A.A.As., D.E.J., J.J.R., and R.R.B. retrieved, cataloged, and prepared mammalian tissue specimens critical to the study. R.R., R.C.P., R.C.N., B.J.B., T.P., A.A.Al., C.-C.Y., M.A.K., E.O.P., Q.N., and M.V.P. analyzed data. L.B.L.-M., R.C.N., B.J.B., J.C.H., J.W.O., C.F.G.-J., S.S., S.I., A.E.Mc., F.v.B., C.-C.Y., S.-J.L., K.L.C., S.E.S., J.E.B., M.K., M.D., D.E.J., A.E.Me., Q.N., T.F.S., M.I.G.-C., K.A.A., and R.R.B. offered critical reviews to the manuscript.

Competing interests: R.R. and M.V.P. are coinventors on a patent application filed by the Regents of the University of California describing the method for producing and purifying human stem cell–derived cartilage cells on the basis of lipid vacuoles, among other claims. K.A.A. and J.C.H. are cofounders of Cartilage Inc. R.C.P. is also affiliated with East Tennessee

State University. R.D. is also affiliated with Morgridge Institute for Research. The authors declare no other competing interests.

Data and materials availability: Mouse bulk RNA-seq data are located at GSE116119. Human bulk RNA-seq data are located at GSE275825. All other data are available in the manuscript or the supplementary materials.

References and Notes

1. M. Kaucka, I. Adameyko, Evolution and development of the cartilaginous skull: From a lancelet towards a human face. *Semin. Cell Dev. Biol.* **91**, 2–12 (2019).
2. A. G. Cole, B. K. Hall, The nature and significance of invertebrate cartilages revisited: Distribution and histology of cartilage and cartilage-like tissues within the Metazoa. *Zoology* **107**, 261–273 (2004).
3. O. A. Tarazona, L. A. Slota, D. H. Lopez, G. Zhang, M. J. Cohn, The genetic program for cartilage development has deep homology within Bilateria. *Nature* **533**, 86–89 (2016).
4. Y. Chai, X. Jiang, Y. Ito, P. Bringas Jr., J. Han, D. H. Rowitch, P. Soriano, A. P. McMahon, H. M. Sucov, Fate of the mammalian cranial neural crest during tooth and mandibular morphogenesis. *Development* **127**, 1671–1679 (2000).
5. M. E. Bronner, N. M. LeDouarin, Development and evolution of the neural crest: An overview. *Dev. Biol.* **366**, 2–9 (2012).
6. B. McBratney-Owen, S. Iseki, S. D. Bamforth, B. R. Olsen, G. M. Morriss-Kay, Development and tissue origins of the mammalian cranial base. *Dev. Biol.* **322**, 121–132 (2008).
7. L. Selleri, F. M. Rijli, Shaping faces: Genetic and epigenetic control of craniofacial morphogenesis. *Nat. Rev. Genet.* **24**, 610–626 (2023).
8. Q. Wang, J. W. Oh, H.-L. Lee, A. Dhar, T. Peng, R. Ramos, C. F. Guerrero-Juarez, X. Wang, R. Zhao, X. Cao, J. Le, M. A. Fuentes, S. C. Jocoy, A. R. Rossi, B. Vu, K. Pham, X. Wang, N. M. Mali, J. M. Park, J.-H. Choi, H. Lee, J. M. D. Legrand, E. Kandyba, J. C. Kim, M. Kim, J. Foley, Z. Yu, K. Kobielak, B. Andersen, K. Khosrotehrani, Q. Nie, M. V. Plikus, A multi-scale model for hair follicles reveals heterogeneous domains driving rapid spatiotemporal hair growth patterning. *eLife* **6**, e22772 (2017).
9. F. Leydig, *Lehrbuch der Histologie des Menschen und der Thiere* (Frankfurt a.M. Meidinger, 1857).
10. C. F. Sanzone, E. J. Reith, The development of the elastic cartilage of the mouse pinna. *Am. J. Anat.* **146**, 31–71 (1976).
11. A. Švajger, Chondrogenesis in the external ear of the rat. *Z. Anat. Entwickl. Gesch.* **131**, 236–242 (1970).
12. R. Mallinger, P. Böck, Differentiation of extracellular matrix in the cellular cartilage ("Zellknorpel") of the mouse pinna. *Anat. Embryol.* **172**, 69–74 (1985).
13. D. R. Anderson, The Ultrastructure of Elastic and Hyaline Cartilage of the Rat. *Am. J. Anat.* **114**, 403–433 (1964).
14. A. E. Lewis, H. N. Vasudevan, A. K. O'Neill, P. Soriano, J. O. Bush, The widely used *Wnt1-Cre* transgene causes developmental phenotypes by ectopic activation of Wnt signaling. *Dev. Biol.* **379**, 229–234 (2013).

15. J. M. Tabler, M. M. Rigney, G. J. Berman, S. Gopalakrishnan, E. Heude, H. A. Al-Lami, B. Z. Yannakoudakis, R. D. Fitch, C. Carter, S. Vokes, K. J. Liu, S. Tajbakhsh, S. R. Egnor, J. B. Wallingford, Cilia-mediated Hedgehog signaling controls form and function in the mammalian larynx. *eLife* **6**, e19153 (2017).
16. R. P. Donahue, R. C. Nordberg, B. J. Bielajew, J. C. Hu, K. A. Athanasiou, The effect of neonatal, juvenile, and adult donors on rejuvenated neocartilage functional properties. *Tissue Eng. Part A* **28**, 383–393 (2022).
17. E. A. Gonzalez-Leon, J. C. Hu, K. A. Athanasiou, Yucatan Minipig Knee Meniscus Regional Biomechanics and Biochemical Structure Support its Suitability as a Large Animal Model for Translational Research. *Front. Bioeng. Biotechnol.* **10**, 844416 (2022).
18. L. W. Huwe, W. E. Brown, J. C. Hu, K. A. Athanasiou, Characterization of costal cartilage and its suitability as a cell source for articular cartilage tissue engineering. *J. Tissue Eng. Regen. Med.* **12**, 1163–1176 (2018).
19 M. M. Yore, I. Syed, P. M. Moraes-Vieira, T. Zhang, M. A. Herman, E. A. Homan, R. T. Patel, J. Lee, S. Chen, O. D. Peroni, A. S. Dhaneshwar, A. Hammarstedt, U. Smith, T. E. McGraw, A. Saghatelian, B. B. Kahn, Discovery of a class of endogenous mammalian lipids with anti-diabetic and anti-inflammatory effects. *Cell* **159**, 318–332 (2014).
20 W. W. Franke, M. Hergt, C. Grund, Rearrangement of the vimentin cytoskeleton during adipose conversion: Formation of an intermediate filament cage around lipid globules. *Cell* **49**, 131–141 (1987).
21 X. He, S. Ohba, H. Hojo, A. P. McMahon, AP-1 family members act with Sox9 to promote chondrocyte hypertrophy. *Development* **143**, 3012–3023 (2016).
22 R. Datta, A. Alfonso-García, R. Cinco, E. Gratton, Fluorescence lifetime imaging of endogenous biomarker of oxidative stress. *Sci. Rep.* **5**, 9848 (2015).
23 R. C. Prince, R. R. Frontiera, E. O. Potma, Stimulated Raman Scattering: From Bulk to Nano. *Chem. Rev.* **117**, 5070–5094 (2017).
24 D. A. Griffith, D. W. Kung, W. P. Esler, P. A. Amor, S. W. Bagley, C. Beysen, S. Carvajal-Gonzalez, S. D. Doran, C. Limberakis, A. M. Mathiowetz, K. McPherson, D. A. Price, E. Ravussin, G. E. Sonnenberg, J. A. Southers, L. J. Sweet, S. M. Turner, F. F. Vajdos, Decreasing the rate of metabolic ketone reduction in the discovery of a clinical acetyl-CoA carboxylase inhibitor for the treatment of diabetes. *J. Med. Chem.* **57**, 10512–10526 (2014).
25 R. U. Svensson, S. J. Parker, L. J. Eichner, M. J. Kolar, M. Wallace, S. N. Brun, P. S. Lombardo, J. L. Van Nostrand, A. Hutchins, L. Vera, L. Gerken, J. Greenwood, S. Bhat, G. Harriman, W. F. Westlin, H. J. Harwood Jr., A. Saghatelian, R. Kapeller, C. M. Metallo, R. J. Shaw, Inhibition of acetyl-CoA carboxylase suppresses fatty acid synthesis and tumor growth of non-small-cell lung cancer in preclinical models. *Nat. Med.* **22**, 1108–1119 (2016).
26 R. Flavin, S. Peluso, P. L. Nguyen, M. Loda, Fatty acid synthase as a potential therapeutic target in cancer. *Future Oncol.* **6**, 551–562 (2010).
27 G. A. Gomez, M. S. Prasad, N. Sandhu, P. B. Shelar, A. W. Leung, M. I. García-Castro, Human neural crest induction by temporal modulation of WNT activation. *Dev. Biol.* **449**, 99–106 (2019).
28 T. Martin, J. Marugán-Lobón, R. Vullo, H. Martín-Abad, Z.-X. Luo, A. D. Buscalioni, A Cretaceous eutriconodont and integument evolution in early mammals. *Nature* **526**, 380–384 (2015).

29 O. R. Bininda-Emonds, M. Cardillo, K. E. Jones, R. D. E. MacPhee, R. M. D. Beck, R. Grenyer, S. A. Price, R. A. Vos, J. L. Gittleman, A. Purvis, The delayed rise of present-day mammals. *Nature* **446**, 507–512 (2007).
30 B. W. Keeley, A. T. H. Keeley, P. Houlahan, Ridge number in bat ears is related to both guild membership and ear length. *PLOS ONE* **13**, e0200255 (2018).
31 H. Liu, L. Witzigreuter, R. Sathiaseelan, M.-P. Agbaga, R. S. Brush, M. B. Stout, S. Zhu, Obesity promotes lipid accumulation in mouse cartilage—A potential role of acetyl-CoA carboxylase (ACC) mediated chondrocyte de novo lipogenesis. *J. Orthop. Res.* **40**, 2771–2779 (2022).
32 S. Park, I. J. Baek, J. H. Ryu, C. H. Chun, E. J. Jin, PPARα–ACOT12 axis is responsible for maintaining cartilage homeostasis through modulating de novo lipogenesis. *Nat. Commun.* **13**, 3 (2022).
33 S. A. O'Leary, N. K. Paschos, J. M. Link, E. O. Klineberg, J. C. Hu, K. A. Athanasiou, Facet Joints of the Spine: Structure-Function Relationships, Problems and Treatments, and the Potential for Regeneration. *Annu. Rev. Biomed. Eng.* **20**, 145–170 (2018).
34 J. Rieppo, J. Töyräs, M. T. Nieminen, V. Kovanen, M. M. Hyttinen, R. K. Korhonen, J. S. Jurvelin, H. J. Helminen, Structure-function relationships in enzymatically modified articular cartilage. *Cells Tissues Organs* **175**, 121–132 (2003).
35 K. A. Athanasiou, R. M. Natoli, *Introduction to Continuum Biomechanics*, Synthesis Lectures on Biomedical Engineering (Springer, 2008).
36 G. Ofek, R. M. Natoli, K. A. Athanasiou, *In situ* mechanical properties of the chondrocyte cytoplasm and nucleus. *J. Biomech.* **42**, 873–877 (2009).
37 C. J. Hunter, J. R. Matyas, N. A. Duncan, Cytomorphology of notochordal and chondrocytic cells from the nucleus pulposus: A species comparison. *J. Anat.* **205**, 357–362 (2004).
38 K. Ellis, J. Bagwell, M. Bagnat, Notochord vacuoles are lysosome-related organelles that function in axis and spine morphogenesis. *J. Cell Biol.* **200**, 667–679 (2013).
39 R. R. Banerjee, S. M. Rangwala, J. S. Shapiro, A. S. Rich, B. Rhoades, Y. Qi, J. Wang, M. W. Rajala, A. Pocai, P. E. Scherer, C. M. Steppan, R. S. Ahima, S. Obici, L. Rossetti, M. A. Lazar, Regulation of fasted blood glucose by resistin. *Science* **303**, 1195–1198 (2004).
40 J. M. Link, J. C. Hu, K. A. Athanasiou, Chondroitinase ABC Enhances Integration of Self-Assembled Articular Cartilage, but Its Dosage Needs to Be Moderated Based on Neocartilage Maturity. *Cartilage* **13**, 672S–683S (2021).
41 S. Picelli, O. R. Faridani, Å. K. Björklund, G. Winberg, S. Sagasser, R. Sandberg, Full-length RNA-seq from single cells using Smart-seq2. *Nat. Protoc.* **9**, 171–181 (2014).
42 J. D. Buenrostro, P. G. Giresi, L. C. Zaba, H. Y. Chang, W. J. Greenleaf, Transposition of native chromatin for fast and sensitive epigenomic profiling of open chromatin, DNA-binding proteins and nucleosome position. *Nat. Methods* **10**, 1213–1218 (2013).
43 M. Minoux, C. F. Kratochwil, S. Ducret, S. Amin, T. Kitazawa, H. Kurihara, N. Bobola, N. Vilain, F. M. Rijli, Mouse *Hoxa2* mutations provide a model for microtia and auricle duplication. *Development* **140**, 4386–4397 (2013).
44 Chen, S. Liao, M. Cheng, K. Ma, L. Wu, Y. Lai, X. Qiu, J. Yang, J. Xu, S. Hao, X. Wang, H. Lu, X. Chen, X. Liu, X. Huang, Z. Li, Y. Hong, Y. Jiang, J. Peng, S. Liu, M. Shen, C. Liu, Q. Li, Y. Yuan, X. Wei, H. Zheng, W. Feng, Z. Wang, Y. Liu, Z. Wang, Y. Yang, H. Xiang, L. Han, B. Qin, P. Guo, G. Lai, P. Muñoz-Cánoves, P. H. Maxwell, J. P. Thiery, Q.-F. Wu, F.

Zhao, B. Chen, M. Li, X. Dai, S. Wang, H. Kuang, J. Hui, L. Wang, J.-F. Fei, O. Wang, X. Wei, H. Lu, B. Wang, S. Liu, Y. Gu, M. Ni, W. Zhang, F. Mu, Y. Yin, H. Yang, M. Lisby, R. J. Cornall, J. Mulder, M. Uhlén, M. A. Esteban, Y. Li, L. Liu, X. Xu, J. Wang, Spatiotemporal transcriptomic atlas of mouse organogenesis using DNA nanoball-patterned arrays. *Cell* **185**, 1777–1792.e21 (2022).